光效能監控及損傷減緩技術

Optical Performance Monitoring and Impairment Mitigation Techniques

研　究　生：蔡坤廷　　Student：Kuen-Ting Tsai

指 導 教 授：尉應時 博士　　Advisor：Winston I. Way

國立交通大學

電信工程研究所

博士論文

A Dissertation
Submitted to the Institute of Communication Engineering
College of Electrical Engineering and Computer Science
National Chiao Tung University
in
Partial Fulfillment of the Requirements
for the Degree of Doctor of Philosophy
in
Electrical Engineering

July 2006

Hsinchu, Taiwan, Republic of China

中華民國九十五年七月

國 立 交 通 大 學

電信工程學系

博 士 論 文

光纖系統監控及效能改進技術

Optical Performance Monitoring and Impairment Mitigation Techniques

研 究 生：蔡坤廷

指導教授：尉應時

中 華 民 國 九十五 年 七 月

光纖系統監控及效能改進技術

研究生：蔡坤廷　　指導教授：尉應時　博士

國立交通大學　電信工程學系

中文摘要

在本論文中，我們提出並驗證三種新穎的技術，適用於光效能監控以及系統的線性化。第一個方法是使用非對稱”馬赫-詹德光濾波器”來做色散監控，適用於高速數位傳輸系統(>40 Gb/s)。另外，無論發射機是否加入導頻載波，或是帶有頻擾(由馬赫-詹德光調變器有限的消光比或是由光纖自我相位調變所造成)，這個方法皆能正常工作。第二個提出的方法可用在 RZ-DPSK 系統中，脈衝產生器和相位調變器間的自動時序調整。主要是利用光學頻率鑑別器來偵測因為時序誤差所造成的光頻譜增寬效應。相較於已知的技術，使用這種方式可以得到較佳的偵測動態範圍，同時不受光極化性質的影響。最後一個方法是使用外調式光發射機的有線電視系統之線性化技術。這個方法同時能夠抑制在傳輸系統上所產生的非線性失真，也可以提高接收端的載波雜訊比。

Optical Performance Monitoring and Impairment Mitigation Techniques

Student: Kuen-Ting Tsai Advisor: Dr. Winston I. Way

Department of Communication Engineering
National Chiao Tung University, Taiwan

Abstract

In this dissertation, we propose and demonstrate three novel techniques for optical performance monitoring (OPM) and impairment mitigation. The first one is proposed for dispersion monitoring at 40 Gb/s or beyond, and is a novel post-detection method based on an optical delay-and-add filter (DAF). The proposed method can be used with or without a pilot tone, and works well even when there exists a residual chirp due to the finite DC extinction ratio of a Mach Zehnder (MZ) modulator or self-phase modulation (SPM). The second technique is proposed and demonstrated for monitoring the timing alignment between a pulse carver and a phase modulator in RZ differential phase shift keying (RZ-DPSK) systems. An optical frequency discriminator is used to monitor the spectrum broadening caused by timing misalignment. After photo-detection, microwave bandpass filtering and envelope detection, a correct timing is achieved by minimizing the detected microwave power. This proposed method has a large detection dynamic range and is polarization independent. Finally, a novel linearization technique is proposed and demonstrated for cable TV (CATV) external-modulated systems, and it can simultaneously suppress the nonlinear distortions (NLDs) generated in a transmission system and increase the received carrier-to-noise ratio (CNR). This technique is based on offsetting the bias voltage of MZ modulator from its inflection point. Both analytical and experimental results are presented for the three techniques.

誌　謝

經過了多年的努力，終於要畢業了。首先，要感謝指導教授尉應時博士多年來的指導與督促，才能讓我的求學生涯更為充實而豐富；同時還要謝謝師母在生活上的關心和照顧。感謝小威學長和翁愷在研究討論中分享珍貴的意見，YM 學長、香港中文大學的陳亮光教授和國偉在實驗上的支援。感謝小郭、豪哥以及潔哥在我不在實驗室那段時間的幫忙，以及 Mika 和戴建學長在工作上的協助。最後也最重要的是感謝我的家人對我的包容、關心和支持。

Table of Contents

List of Figures

Chapter 1 Overview

Generally speaking, the impairments caused by imperfections in an all-optical network will accumulate along the optical path through the network, and the signal quality will become unacceptable after some distance. Therefore, there will be transmission limitations in all-optical networks. Optical impairments which degrade the signal quality can be classified into three broad categories [1].

(a) **Noise**: random signal fluctuations that are often treated as a Gaussian process and can be signal level dependent. Examples are optical amplifier noise and laser noise.

(b) **Distortion**: modification of the average signal waveform, for example, the average waveform of the marks and spaces taken separately. Distortion is caused by nonlinearities or fiber dispersion effects and may be signal level and pattern dependent and can lead to burst errors and BER floors. Examples include laser, optical amplifier and fiber nonlinearities, laser diode bit pattern dependent response, receiver bit pattern dependent response, chromatic and polarization mode dispersion, and phase induced intensity noise.

(c) **Timing**: fluctuations in the time registration of the bits. Timing jitter can occur as quickly as bit-to-bit or accumulate over many bit periods.

In order to achieve long link lengths, many well-known and perhaps countable deleterious effects of optical transmission must be minimized or controlled carefully, and all of these effects are controlled through the network design. The transmission margin is ensured to be enough, while the worst-case impacts of transmission impairments are taken into consideration in the network design. Notable transmission impairments include [1]

(a) Amplifier noise

(b) Amplifier distortion and transients

(c) Chromatic dispersion (CD)

(d) Polarization–mode dispersion (PMD)

(e) Fiber nonlinearity induced distortion and crosstalk (self-phase modulation (SPM), cross-phase modulation (XPM), four-wave mixing (FWM), stimulated Raman scattering (SRS), and stimulated Brillouin scattering (SBS).

(f) Timing jitter

(g) Polarization effects

(h) Interference effects (MPI)

(i) Pump laser RIN transfer

(j) Optical filter distortion

(k) Linear crosstalk

As the network capacity increases, the above factors reduce the window of operability further. Therefore, new technologies have been developed to keep the window open, and optical performance monitoring (OPM) and impairment mitigation techniques are potential means of widening this window. These techniques can improve the control of transmission and physical layer fault management, and they are essential in building a high capacity and reliable all-optical network, which are expected to be transparent and dynamically reconfigurable. In future optical networks, OEO conversion will be mostly eliminated, and therefore the bit-rate-, modulation-format-, and protocol- independent performance monitoring and impairment mitigation techniques are required. Moreover, wavelength channels are added to and dropped from optical nodes dynamically, and these techniques have to be without knowledge of the origin or transport history of data stream. Using maintenance calls to manually adjust optical components or network elements is not practical, so the monitored signals are needed for impairment compensation or fault correction. These reconfigurable properties in all-optical networks will drive the need for adaptive compensation techniques, such as chromatic dispersion and PMD equalization.

Historically, performance monitoring refers to monitoring at SONET/SDH layer, and each data stream will be recovered at every network node. The optical

performance monitoring started to be paid attention, while people think more about optical network rather than optical transmission. The purpose of OPM is to examine the signal quality in the optical domain, and the broad spectrum of OPM includes a plethora of parameters to be monitored which can be classified into three categories as shown in the Fig. 1.2 [2].

(a) **Signal loss monitoring**: refers to the monitoring of in-line component failures and fiber cuts that cause a change in opacity in optical transmission. It is particularly important to monitor the active components such as EDFA and optical crossconnects due to their high failure probability.

(b) **Signal alignment monitoring**: on the other hand, concerns with the alignment of signal wavelength, filter position, and pulse carver to ensure proper operation.

(c) **Signal quality monitoring**: pertains to the monitoring of a multitude of disparaging effects that must be minimized or controlled. These impairments include noise, distortion, and timing jitter.

The OPM techniques can either be digital or analog. High-speed processor is used in digital techniques to recover bits embedded on optical waveforms, and high correlation with bit error rate (BER) can be obtained. However, digital methods can not isolate the effects of individual impairments effectively. Analog waveforms are measured and analyzed directly in analog methods, so analog measurement are typically protocol-independent. Analog measurements can be subdivided further into time domain and spectrum methods. The time domain methods includes eye diagram and auto-correlation measurements, and the spectrum methods includes optical spectrum and RF spectrum measurements.

Compared to time domain methods, the spectrum techniques can be implemented by narrowband electronics, so it is less complicated and cost effective, even high frequency subcarriers are involved. In addition, the monitoring sensitivity may be increased as well, because narrow detection bandwidth is used. High sensitivity is of importance for optical monitoring, because the optical power levels for monitoring is usually quite small.

Indeed, performance monitors that provide feedback for closed loop control of compensation elements will be desirable for management systems to mitigate or compensate the degrading effects, and this OPM combination might be implemented with little additional hardware. Real time performance monitors can measure the signal quality, and the monitored signal will be used to trigger alarms and feedback to active compensators adaptively. As a result, the impairments caused by component aging, fiber degradation or environmental changes will be controlled or mitigated, and therefore system reliability is guaranteed.

In this dissertation, we will focus on performance monitoring and impairment mitigation techniques related to (1) chromatic dispersion monitoring and equalization, (2) pulse carver and data alignment monitoring, and (3) electro-optical pre-distortion technique. For high-speed wavelength division multiplexed (WDM) systems, the system performance is strongly affected by fiber chromatic dispersion and fiber nonlinearity. In a re-configurable WDM network, the accumulated chromatic dispersion of each channel may change frequently. To achieve full dispersion compensation, a variable dispersion compensator (VDC) is needed to optimize the residual dispersion for each channel. Moreover, the chromatic dispersion is sensitive to ambient temperature, and this variation would harm the high-speed signals greatly. So, the online automatic chromatic dispersion equalization techniques become indispensable in high-speed WDM systems.

The combination of the two modulators for the pulse carving and data modulation poses the problem of maintaining the correct timing of two devices. Since the optical path length in between depending on the ambient temperature, the bit-synchronous modulation is easily asynchronized. Accordingly, to drive phase modulator synchronously with the pulse sequence, the clock timing alignment is essential for bit-synchronous modulation, such as RZ (return-to-zero) and CS-RZ (carrier-suppressed RZ), which use two optical modulators for data and clock, respectively.

Duo to the stringent carrier-to-noise ratio (CNR) requirement of analog AM-VSB signals, semiconductor optical amplifiers (SOAs) have long been considered not suitable for CATV systems which transmit multi-channel AM-VSB signals. This is because the amplifier's nonlinear distortion (NLD), which is caused by signal-induced carrier density modulation, can potentially degrade system performance seriously, and can not be accepted by AM-VSB signals. As a result, linearization techniques to improve SOA saturation characteristic and thereby to

expand the SOA input power dynamic range are attractive for CATV systems.

This dissertation is organized as follows. Chapter 2 describes the dispersion monitoring that we propose for high-speed transmission systems at 40 Gb/s or beyond, and it is a novel post-detection method based on an optical delay-and-add filter (DAF). The proposed method can be used with or without a pilot tone, and works well even when there exists a residual chirp due to the finite DC extinction ratio of a Mach Zehnder modulator or self-phase modulation. In Chapter 3, a novel technique for monitoring the timing alignment between a pulse carver and a phase modulator in RZ-DPSK systems is proposed and demonstrated. An optical frequency discriminator is used to monitor the spectrum broadening caused by timing misalignment. Chapter 4 describes a novel linearization technique for CATV external-modulated systems, and it can simultaneously suppress the nonlinear distortions (NLDs) generated in a transmission system and increase the received carrier-to-noise ratio (CNR). Both analytical and experimental results are presented. Finally, conclusions and future works are drawn in Chapter 5.

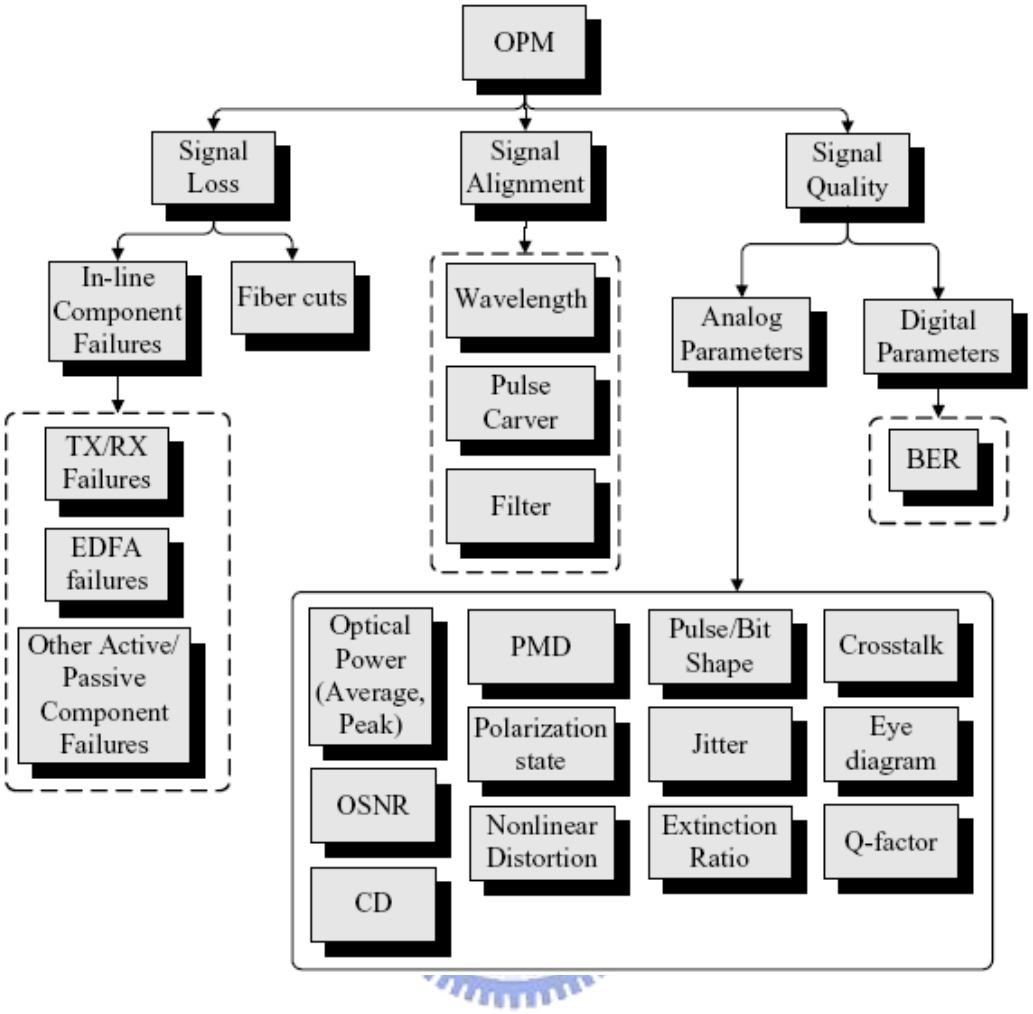

Fig. 1.1 The broad spectrum of OPM [2]

Chapter 2 Chromatic Dispersion Monitoring and Equalization

2.1 Introduction

Online automatic dispersion equalization techniques are indispensable for long-haul, high-speed DWDM systems. A dispersion equalizer has two important design parameters, i.e., dispersion monitoring window and dispersion resolution. Dispersion monitoring window is important because a large chromatic dispersion variation could be incurred due to a wide ambient temperature change. For example, assuming that the temperature dependence of a zero-dispersion wavelength and the dispersion slope of a 500 km optical fiber system are 0.03 nm/^{o}C and 0.08 ps/nm^{2}/km, respectively, a temperature change of 40^{o}C could induce a large dispersion variation of 48 ps/nm. This variation could be even larger for longer transmission distances. Dispersion resolution is of special importance for data rates higher than 40 Gb/s, because a small chromatic dispersion of 60 and 15 ps/nm can cause 1 dB power penalty in 40 and 80 Gb/s NRZ systems. Modulation formats such as RZ and carrier-suppressed RZ (CS-RZ) have even smaller dispersion tolerance, e.g., 40 Gb/s RZ and CS-RZ incur a 1 dB power penalty at a chromatic dispersion of 30 ps/nm [3] and 25 ps/nm [4], respectively.

In a linear dispersion compensation scheme, residual fiber dispersion could be fully compensated via either a pre-detection or a post-detection scheme in combination with a variable dispersion compensator (VDC) at a receiver, as illustrated in Fig. 2.1. In a pre-detection scheme, a dispersion detector first detects the total chromatic dispersion in a transmission system, and followed by a VDC whose dispersion is adjusted to be the same as the measured total system dispersion but with a negative sign. Examples of pre-detection schemes include the use of an amplitude modulation (AM) pilot tone [5],[6] and clock fading technique [7]–[10]. In a post-detection scheme, a zero-dispersion detector is used to monitor the residual dispersion. The zero-dispersion detector generates a VDC control signal so that the VDC can completely cancel the residual dispersion. Examples of post-detection schemes include PM pilot tones [6], [11], off-line alternating chirp [12], and clock generation techniques [7], [9], [10].

Each of above monitoring techniques have one or more of the following

disadvantages [4]:

(a) Monitored physical quantity is influenced not only by chromatic dispersion but also by other effects, such as PMD and nonlinearities.

(b) Tansmitter/receiver must be modified.

(c) Monitoring range and sensitivity are low or modulation format dependent.

(d) Implementation is complex and may require stabilization.

(e) A single monitor can only accommodate a single wavelength.

The advantages of our proposed technique include:

(a) Insensitivity to SPM and PMD.

(b) No modification of the transmitter. Thus, the transmitted waveform will not be distorted, and no extra spectrum will be occupied.

(c) Large monitoring range and high sensitivity.

(d) Easy to implement and an adaptive feedback scheme is proposed to stabilize DAF.

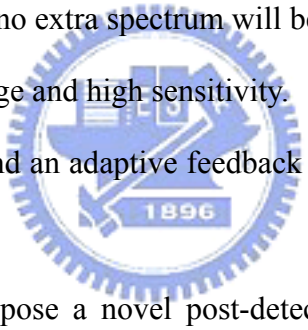

In this Chapter, we propose a novel post-detection technique which exhibits both sufficient monitoring window and high dispersion resolution. The technique uses an optical delay-and-add filter (DAF), in combination with (a) an AM pilot tone or (b) any modulation format which has a symmetric spectrum with respect to its optical carrier (e.g., NRZ, RZ, CS-RZ, RZ differential phase shift keying (RZ-DPSK), CSRZ-DPSK, etc.). A DAF is basically an asymmetric Mach Zehnder interferometer (AMZI) with a differential optical delay τ between the two arms. The DAF used in our proposal has a nominal delay that is equal to a half period of an AM pilot tone, or a half-bit/one-bit period of a high-speed modulating data when there is no pilot tone.

This Chapter is organized as follows. Section 2.2 describes the operation principle of an AM pilot tone-based post-detection scheme using DAF. The impacts of the detuning of the differential optical delay and the frequency misalignment between the monitored optical wavelength and the DAF are investigated. A filter tuning and stabilization scheme for the DAF is also proposed. In Section 2.3, the

operation principle of the post-detection scheme using DAF filtering without a pilot-tone is presented. In Section 2.4, the conventional RZ format without a pilot tone is used to demonstrate the spectrum properties and waveform distortions after DAF filtering. We will prove that the proposed technique works even when fiber chromatic dispersion interacts with frequency chirp caused by self-phase modulation (SPM) or by a finite DC extinction ratio of a MZ modulator. The same detection technique (without adding a pilot-tone) is used for NRZ, RZ, CS-RZ, RZ-DPSK and CSRZ-DPSK. Finally, the experimental results are presented in Section 2.5.

2.2 Operation Principle of Proposed AM-Pilot-Tone-Based Post-Detection Scheme Using DAF

A simplified system model is considered in Fig. 2.2. An optical source (denoted by its electric field $s(t)$, representing a CW laser externally modulated by an AM pilot tone with a frequency f_p) is launched into a dispersive fiber with a transfer function $H_{fiber}(f)$. Only linear dispersion effect is taken into account in this section. The signal at the end of the transmission link is coupled into a DAF, whose constructive or destructive output port has a transfer function $H_+(f)$ or $H_-(f)$. The received $r_+(t)$ or $r_-(t)$ after the DAF is converted to a photo-current $i(t)$. It should be noted that the actual modulating data does not pass through DAF, only the post-detection path passes through the DAF via a tap coupler as shown in Fig. 2.1(b). The Fourier transforms of all signals are also shown in Fig. 2.2. Note that we ignore the effect of baseband modulation in our calculation because we assume any intermodulation product caused by the beating between the baseband data and the pilot tone would have amplitude much smaller than that of the pilot tone. The effect of pilot tone on data can be small [5], and is not within the scope of this Chapter.

It is well known that after a transmission link and a photo-receiver (without DAF), the magnitude of an AM pilot tone will change with the total accumulated dispersion of the optical link. This is because optical fiber dispersion causes a time delay (and thus relative phase change) between the transmitted upper- and lower-sideband AM pilot tones. Consequently, in a pre-detection scheme we can estimate the total accumulated dispersion by measuring the magnitude of the received pilot tone. The detected chromatic dispersion-dependent RF power of an AM pilot tone can be expressed as [13]

$$P_{AM} = \frac{1}{2}\left\{\Re P_o m\left|\cos\left(\frac{\pi\lambda^2 DL}{c} f_p^2\right)\right|\right\}^2 R_L \qquad (2\text{–}1)$$

where $\Re$ is the responsivity, R_L is the resistive load of the optical receiver, P_o is the average received optical power, m is the *rms* modulation index of the AM pilot tone, c is the speed of light in vacuum, λ is the operating wavelength, D is the fiber dispersion parameter, and DL is the total accumulated dispersion. When the accumulated dispersion is small, the magnitude of the AM pilot tone remains almost constant, and as a result, the frequency of the pilot tone needs to be increased to improve the resolution sensitivity ($\Delta P_{\mathrm{AM}}/\Delta DL$, in dB/(ps/nm)). This out-of-band

pilot tone requires a higher bandwidth photo-detector, costly microwave/millimeter-wave components, and reduces the effective system spectral efficiency.

To improve the problems explained above, we use an optical DAF before a photo-detector, as shown in Figs. 2.2 and 2.3. The frequency response of the constructive port of the DAF can be written as

$$H_+(f) = |H_+(f)|e^{j\Phi_+(f)} = \frac{j}{2}(e^{-j2\pi\tau f} + 1) \qquad (2\text{–}2)$$

Fig. 2.4 illustrates the magnitude and phase response of the DAF at the constructive port, and the frequency spectrum of an optical carrier (f_o) and its associated AM pilot tones ($f_o + f_p$ and $f_o - f_p$). The free spectral range (FSR) of the DAF is $1/\tau$. The basic idea is to let the phase shifts between the optical carrier and the two pilot-tone sidebands be $+\pi/2$ and $-\pi/2$, respectively, so that these two sidebands have a π phase difference and therefore they could cancel each other (i.e., the received AM pilot tone amplitude is zero) when there is zero fiber dispersion. In addition, the received pilot tone power should change significantly even when only a small residual dispersion is incurred, so that a high dispersion resolution can be obtained. These goals can be achieved when two conditions are satisfied:

(1) $\tau = \tau_o = 1/(2f_p)$;

(2) The left-hand-side pilot tone, the optical carrier, and the right-hand-side pilot tone are aligned with three successive quadrature points of $|H_+(f)|^2$, as shown in Fig. 2.4, which implies

$$f_o = \frac{2n-1}{4\tau} \qquad (2\text{–}3)$$

where n is an integer. The amplitudes and phases of the three frequency components in Fig. 2.4 can be verified by substituting f in (2–2) with $f_o + 1/(2\tau_o)$, f_o, and $f_o - 1/(2\tau_o)$, respectively, and use the two conditions given above. As a result, the optical carrier and the two pilot tones all experience a 3 dB optical power loss.

It should be noted that in practical systems, τ may deviate away from τ_o, i.e., $\tau = \tau_o + \delta\tau$. This can be observed from the above two conditions that $\tau_o = 1/(2f_p)$ and $\tau = (2n-1)/(4f_o)$ cannot be always equal for any arbitrary f_o , f_p and n. As a matter of fact, f_o is always given, while τ needs to be adjusted such that condition (2) is always

satisfied, but not necessarily condition (1). For example, if f_o = 193.3 THz, f_p = 40 GHz, we obtain $\tau = \tau_o$ = 1/(2f_p) = 12.5ps, and (2–3) is satisfied by letting n equal to 4833. But when the optical carrier frequency is changed to f_o = 191.123 THz, (2–3) is satisfied by letting n equal to 4799 and $\tau \approx$ 12.501ps, i.e., $\tau \neq \tau_o$ in this case. We will show the effect of $\delta\tau$ in Fig. 2.5, Fig. 2.6, and (2–13).

The electric field of a pilot tone after passing through a dispersive fiber and a DAF can be written as

$$r_+(t) = \sqrt{P_o}\, H_1 e^{j\phi_1}\, e^{j\Omega_0 t} \left\{ 1 + \frac{m}{4}\left(\frac{H_2 + H_3}{H_1}\right) e^{j\left(qf_p^2 - \phi_1 + \frac{\phi_2+\phi_3}{2}\right)} \cos\left(\omega_p t + \frac{\phi_2 - \phi_3}{2}\right) + j\frac{m}{4}\left(\frac{H_2 - H_3}{H_1}\right) e^{j\left(qf_p^2 - \phi_1 + \frac{\phi_2+\phi_3}{2}\right)} \sin\left(\omega_p t + \frac{\phi_2 - \phi_3}{2}\right) \right\} \tag{2–4}$$

where

$$q = -2\pi^2 \beta_2 L = \frac{\pi\lambda^2 DL}{c} \tag{2–5}$$

$$\begin{aligned} H_1 &= \left|H_+(f_o)\right| = \left|\cos(\pi\tau\, f_o)\right| \\ H_2 &= \left|H_+(f_o + f_p)\right| = \left|\cos\left[\pi\tau(f_o + f_p)\right]\right| \\ H_3 &= \left|H_+(f_o - f_p)\right| = \left|\cos\left[\pi\tau(f_o - f_p)\right]\right| \end{aligned} \tag{2–6}$$

and

$$\begin{aligned} \phi_1 &= \Phi_+(f_o) = -\pi\tau\, f_o + \frac{\pi}{2} + \angle\cos(\pi\tau\, f_o) \\ \phi_2 &= \Phi_+(f_o + f_p) = -\pi\tau\, f_o + \frac{\pi}{2} + \angle\cos\left[\pi\tau(f_o + f_p)\right] - \pi\tau\, f_p \\ \phi_3 &= \Phi_+(f_o - f_p) = -\pi\tau\, f_o + \frac{\pi}{2} + \angle\cos\left[\pi\tau(f_o - f_p)\right] + \pi\tau\, f_p \end{aligned} \tag{2–7}$$

The photo-current of f_p is obtained by squaring (2–4) and keeping the linear terms at the modulation frequency f_p :

$$i_{AM,DAF}(t) = \Re P_o \frac{m}{2} H_1 \sqrt{(H_2+H_3)^2 \cos^2\left(qf_p^2 - \phi_1 + \frac{\phi_2+\phi_3}{2}\right) + (H_2-H_3)^2 \sin^2\left(qf_p^2 - \phi_1 + \frac{\phi_2+\phi_3}{2}\right)} \cdot \cos\left(\omega_p t + \frac{\phi_2-\phi_3}{2} + \theta\right) \tag{2–8}$$

where $\theta = \tan^{-1}\left\{\frac{(H_2-H_3)\sin\left(qf_p^2 - \phi_1 + \frac{\phi_2+\phi_3}{2}\right)}{(H_2+H_3)\cos\left(qf_p^2 - \phi_1 + \frac{\phi_2+\phi_3}{2}\right)}\right\}$ (2–9)

After some mathematical manipulations, it follows that the transfer function of the cascade of a dispersive fiber and a DAF is given by

$$H_{fib,DAF}(f_o, f_p, \tau, q) = \left|\cos(\pi\tau f_o)\right| \sqrt{\sin^2(\pi\tau f_o)\sin^2(\pi\tau f_p)\sin^2(qf_p^2) + \cos^2(\pi\tau f_o)\cos^2(\pi\tau f_p)\cos^2(qf_p^2)} \tag{2–10}$$

Consequently, the detected RF power of the AM pilot tone after a dispersive transmission link and a DAF can be expressed as

$$P_{AM,DAF} = \frac{1}{2}\left\{\Re P_o m H_{fib,DAF}(f_o + f_p, \tau, q)\right\}^2 R_L \tag{2–11}$$

When $\tau = \tau_o$ and (2–3) are both satisfied, (2–11) can be simplified as

$$P_{AM,DAF} = \frac{1}{2}\left\{\Re P_o m K^2 \left|\sin\left(\frac{\pi\lambda^2 DL}{c} f_p^2\right)\right|\right\}^2 R_L \tag{2–12}$$

where $K = \frac{1}{\sqrt{2}}$ is the transmittance of the DAF at the wavelength of the pilot-tone sidebands. Comparing (2–12) to (2–1), we see that the amplitude of the pilot-tone is now related to a sinusoidal function, rather than a cosine function, of the accumulated dispersion. Therefore, the dispersion resolution can be improved significantly around zero dispersion. Note that this sinusoidal dependence on fiber dispersion is similar to those dispersion equalization techniques which utilize PM pilot tone [6],

[11]. The main difference lies in the fact that [6] used a serial PM modulator at the transmitter, [11] used a parallel PM modulator at the transmitter, while this Chapter used an AMZI at the receiver. Therefore, the proposed method in this Chapter has the same advantages mentioned in [6], such as SPM and PMD-tolerant. In terms of complexity, the proposed method is not more complicated than those shown in [6], [11] — those papers have a complicate transmitter design with excessive power loss, while this Chapter has an extra AMZI at the receiver (note that the tapped loss can be easily compensated by an existing pre-amplifier). It is also noted that DAFs have been widely used in optical DPSK demodulation, and are commercially available with thermally tunable optical delay.

As we mentioned previously, there always will be an unavoidable delay variation $\delta\tau$ in practical conditions. Its effect on an AM pilot-tone RF power at different accumulated fiber dispersion *DL* can be examined by substituting $\tau f_o = (2n\text{-}1)/4$, $\tau = \tau_o + \delta\tau$ and $\tau_o = 1/(2f_p)$ into (2−11) (i.e., condition (2) in Section 2.2 is satisfied, while condition (1) is not):

$$P_{AM,DAF} = \frac{1}{2}\left\{\Re P_o m \frac{1}{2}\sqrt{\cos^2(\pi\delta\tau\, f_p)\sin^2(qf_p^2) + \sin^2(\pi\delta\tau\, f_p)\cos^2(qf_p^2)}\right\}^2 R_L \qquad (2\text{−}13)$$

Based on (2−13), Fig. 2.5 shows the AM pilot-tone power as a function of the normalized delay variation $\delta\tau/\tau_0$ at different total residual dispersion *DL* (0, 0.05, 0.5, 5 and 20 ps/nm), and $\Re$=1, P_o=0.5 mW, m=0.16, f_o=193.3 THz, f_p=40 GHz, R_L=1. We can see that the maximum AM pilot tone power always occurs at quadrature points of the DAF power transfer function (i.e., $\delta\tau/\tau_o$ = 0, ±0.021%, ±0.042%, etc.) when $DL \neq 0$, and the higher the residual dispersion *DL*, the higher the AM pilot tone power. The maximum AM pilot-tone power at ±0.021%, ±0.042%, etc., can be explained as follows: As previously discussed, n = 4833 in (2–3) when $\tau = \tau_o = 1/(2f_p) = 12.5$ps. The two nearest quadrature points take place at n = 4832 and 4834, respectively. As a result, $\delta\tau/\tau_o$ = (4834-4833)/4833 or (4832-4833)/4833) = ±0.021% if f_o is shifted to any of the two neighbor quadrature points. When *DL*=0, the residual AM pilot tone power is not completely zero except at several points such as $\delta\tau/\tau_o$=0. The non-zero residual AM pilot tone power at *DL*=0 originates from the $cos^2(qf_p^2)$ term in the square root of (2−10) or (2−13).

Fig. 2.5 shows a small variation range (within ±0.1%) of $\delta\tau/\tau_o$, which means τ_o is very closely matching $1/(2f_p)$ (this section), or a half of the data-bit-period (Section 2.3). However, sometimes due to fabrication uncertainties of τ in AMZI, and

sometimes due to data rate changes after line coding, there may be a large variation range of $\delta\tau/\tau_o$. In Fig. 2.6, the solid lines are the calculated pilot-tone power as a function of residual dispersion over a much larger variation range of $\delta\tau/\tau_o$ (up to 18.75%) based on (2−13). In Fig. 2.6, the frequencies of the pilot tone and optical carrier are 40 GHz and 193.3 THz, respectively; and $\delta\tau/\tau_o$ is set to 0% (open triangle), 6.25% (open circle), 12.5% (open diamond), and 18.75% (open square), respectively. Fig. 2.6 also shows that the smaller $\delta\tau/\tau_o$, and the smaller the residual dispersion, the higher the dispersion resolution around zero accumulated dispersion. In addition, we see that the monitoring window is ±39 ps/nm in the 40 GHz pilot tone-based systems. This monitoring window is sufficient compared to other detection schemes [5−10]. Fig. 2.6 also shows the simulation data (in various symbols) based on VPItransmission Maker. The key simulation parameters are shown in the figure caption of Fig. 2.6. We can see that these simulation results match well with the theoretically calculated results except that there is a small discrepancy at a normalized delay variation of 0%. This because the simulation took into account the residual chirp in a transmitter MZ modulator due to its limited extinction ratio of 40 dB, while (2−13) does not consider the residual chirp. Fig. 2.6 also shows that a small monitoring error of 10 ps/nm due to SPM is incurred when the fiber launched power is increased from -3 dBm/ch to 12 dBm/ch. As mentioned previously, SPM- and PMD-induced monitoring error can be reduced by lowering the pilot tone frequency, same as the PM-pilot-tone method.

As was shown in Fig. 2.5, the maximum AM pilot tone power always occurs at the quadrature points of a DAF power transfer function when $DL \neq 0$. Consequently, the DAF differential delay τ should always be adjusted to let the monitored optical wavelength coincide with one of the DAF quadrature points (i.e., condition 2 (Eq.(2−3)) in Section 2.2 is always satisfied, but not necessarily condition 1). We show in Fig. 2.3 a DAF control loop which can be used to achieve this purpose. This control loop uses a differential optical power detection method which is similar to those commonly adapted for wavelength stabilization [14]. The DC optical power detected at the constructive and destructive ports are

$$P_+ = P_o\left|H_+(f_o)\right|^2 = P_o\left|\cos(\pi\tau f_o)\right|^2 = \frac{P_o}{2}\left\{1+\cos\left[2\pi\tau_o f_o\left(1+\frac{\delta\tau}{\tau_o}\right)\right]\right\} \qquad (2-14)$$

and

$$P_{-} = P_o |H_{-}(f_o)|^2 = P_o |\sin(\pi\tau f_o)|^2 = \frac{P_o}{2}\left\{1 - \cos\left[2\pi\tau_o f_o\left(1+\frac{\delta\tau}{\tau_o}\right)\right]\right\} \quad (2\text{–}15)$$

respectively, where $H_{+}(f)$ was defined in (2–2), and $H_{-}(f)$ is the frequency response of the DAF destructive port given by

$$H_{-}(f) = |H_{-}(f)|e^{j\Phi_{-}(f)} = \frac{1}{2}(e^{-j2\pi tf} - 1) \quad (2\text{–}16)$$

The error signal used to stabilize the DAF in Fig. 2.3 is

$$E = \frac{P_{+} - P_{-}}{P_{+} + P_{-}} = \cos(2\pi\tau f_o) = \cos\left[2\pi\tau_o f_o\left(1+\frac{\delta\tau}{\tau_o}\right)\right] \quad (2\text{–}17)$$

It follows that the zero-crossings of the error signal occur at

$$\tau = \frac{2n-1}{4f_o} \quad (2\text{–}18)$$

where n is an integer. This is exactly the same as (2–3). Note that the control loop uses only the DC optical power of the DAF constructive and destructive ports, and is independent of the signal modulation format or data rate.

2.3 Proposed DAF Zero-Dispersion Detection without a Pilot-Tone

In this Section, we will show that the DAF post-detection method can also be applied to any modulation formats with symmetrical spectrum (e.g., NRZ, RZ, CS-RZ, RZ-DPSK, CSRZ-DPSK, etc.). The key point is that when $DL \neq 0$ a clock component $|I(f_c)|$ should be generated, and when $DL=0$, the clock component should be zero. The DAF used in this Section is different from that in Section 2.2 in that the differential delay in AMZI is $1/(2f_c)$ ($=T/2$, where T is the data period) instead of $1/(2f_p)$. It should be noted that in Section 2.2, the pilot tone frequency f_p can be adjusted by a user; while in this section, f_c is the clock frequency of the modulating data, which cannot be changed.

Let us assume that the transmitted electric field s(t) can be expressed as

$$s(t) = x(t)\, e^{j\Omega_o t} \tag{2–19}$$

where $x(t)$ is the envelope of the electric field, and is given by

$$x(t) = \frac{\sqrt{P_o}}{2}\left[1 + \sum_n I_n g(t - nT)\right] \quad \text{(for ASK)} \tag{2–20}$$

or

$$x(t) = \sqrt{P_o}\sum_n I_n g(t - nT) \quad \text{(for PSK)} \tag{2–21}$$

where $\{I_n\}=\{\pm 1\}$ is the transmitted data sequence, T is the data period, and $g(t)$ is the pulse shape. From (2–19), we have $S(f) = X(f - f_o)$, where $S(f)$ is the Fourier Transform of $s(t)$. $S(f)$ is symmetric with respect to the frequency of the optical carrier, i.e.,

$$\begin{aligned} &|S(f_o + f)| = |S(f_o - f)| \\ &\phi_s(f_o + f) = -\phi_s(f_o - f) \\ &\text{where } S(f) = |S(f)|\, e^{j\phi_s(f)} \end{aligned} \tag{2–22}$$

We will need to use this symmetric property in deriving (2–29) later on.

The received optical signal spectrum before a photo-detector is given by

$$R_+(f) = H_+(f)H_{fiber}(f)S(f) = |H_+(f)||S(f)|\, e^{j\{\phi_+(f)+\phi_{fiber}(f)+\phi_s(f)\}} \qquad (2\text{–}23)$$

where $H_+(f)$ is the transfer functions of a DAF (given by (2–2), but with τ replaced by $T/2$), and $H_{fiber}(f)$ is the transfer function of a dispersive fiber system. The spectrum of the photo-current is then given by

$$I(f) = R_+(f) \otimes R_+^*(-f) = \int_{f_o-\frac{1}{2}f_{WDM}}^{f_o+\frac{1}{2}f_{WDM}} R_+(\nu)R_+^*(f+\nu)d\nu \qquad (2\text{–}24)$$

where ⊗ denotes the convolution operation and f_{WDM} is the bandwidth of a WDM filter. The clock frequency component at f_c is resulted from the sum of all beats between any two frequency components whose spacing is f_c in the optical spectrum, and is given by (with a change of variable $\nu' = \nu + f_c/2 - f_o$ in (2–24))

$$\begin{aligned} I(f_c) &= \int_{-\frac{1}{2}f_{WDM}+\frac{1}{2}f_c}^{\frac{1}{2}f_{WDM}+\frac{1}{2}f_c} R_+(f_o+f-\frac{f_c}{2})R_+^*(f_o+f+\frac{f_c}{2})df \\ &= \int_0^{\frac{1}{2}f_{WDM}-\frac{1}{2}f_c}\left[R_+(f_o-f-\frac{f_c}{2})R_+^*(f_o-f+\frac{f_c}{2}) + R_+(f_o+f-\frac{f_c}{2})R_+^*(f_o+f+\frac{f_c}{2})\right]df \end{aligned} \qquad (2\text{–}25)$$

Since $R_+(f)$ is composed of $H_+(f)$, $H_{fiber}(f)$, and $S(f)$, if we can use their amplitude and phase symmetry/anti-symmetry properties (with respect to f_o), and prove that the two terms in (2–25) are equal and 180° out-of-phase at DL=0, then the usefulness of DAF detection method is proven. The amplitude and phase responses of the DAF at the constructive port, respectively, can be expressed as

$$\begin{aligned} \left|H_+(f_o+f-\frac{f_c}{2})\right| &= \left|H_+(f_o-f-\frac{f_c}{2})\right| = \left|\cos(\pi\tau_o f)\right| \\ \left|H_+(f_o+f+\frac{f_c}{2})\right| &= \left|H_+(f_o-f+\frac{f_c}{2})\right| = \left|\sin(\pi\tau_o f)\right| \end{aligned} \qquad (2\text{–}26)$$

and

$$\phi_+(f_o+f+\frac{f_c}{2})-\phi_+(f_o+f-\frac{f_c}{2})=\phi_+(f_o-f-\frac{f_c}{2})-\phi_+(f_o-f+\frac{f_c}{2})=\theta_+ \quad \text{where } \theta_+=90°\,or\,-90° \tag{2–27}$$

Note that (2–27) is consistent with the concept presented in Fig. 2.4 where we have shown that any two frequencies with a difference of f_c (i.e., 0.5FSR) have a phase difference of 90^o or -90^o. The amplitude response of a dispersive fiber is constant and its transfer function can be expressed as

$$\begin{aligned} H_{fiber}(f_o+f+\frac{f_c}{2}) &= H_{fiber}(f_o-f-\frac{f_c}{2})=e^{jq\left(f+\frac{f_c}{2}\right)^2} \\ H_{fiber}(f_o+f-\frac{f_c}{2}) &= H_{fiber}(f_o-f+\frac{f_c}{2})=e^{jq\left(f-\frac{f_c}{2}\right)^2} \end{aligned} \tag{2–28}$$

Therefore, after substituting (2–22), (2–26), (2–27) and (2–28) into (2–25), we can obtain the complex frequency component of the detected signal at f_c as

$$I(f_c)=\int_0^{\frac{1}{2}f_{WDM}-\frac{1}{2}f_c}\left[\left|\sin(2\pi\tau_o f)\right|S(f_o+f+\frac{f_c}{2})\left\|S(f_o+f-\frac{f_c}{2})\right|e^{j\left[\phi_s(f_o+f-\frac{f_c}{2})-\phi_s(f_o+f+\frac{f_c}{2})\right]}\cos(\theta_++2qf_cf)\right]df \tag{2–29}$$

It follows that the magnitude of the complex frequency component at f_c, $|I(f_c)|$, is zero if the total accumulated dispersion DL is zero because the cosine term in (2–29) is zero (when DL=0, we have q=0 according to (2–5), and θ_+ is either 90^oor -90^o) . Note that this result could be achieved for any real modulating signal which has a symmetric amplitude property (and anit-symmetric phase characteristic) with respect to its optical carrier. The simple physics can again be summarized as follows: Since the clock component generated from the beating of any two frequency components with a frequency difference of f_c could result in a phase of $+90^o$ or -90^o, the resultant clock power after a photo-detector is zero when DL=0, because the number of contributing terms to $+90^o$ or -90^o are equal. When $DL\neq0$, however, the upper and lower sideband clock frequencies experience different phase rotations due to the fiber dispersion, the 180^o phase relationship no longer exists and therefore the resultant clock power after a photo-detector is not zero.

In the case that the modulation formats with asymmetric frequency response are

applied, such as an optical single sideband (OSSB) signal, the double sideband AM pilot tone-based DAF detection technique (Section 2.2) can be used.

We use an RZ50 signal, which has symmetrical spectrum with respect to an optical carrier, as an example to show the effectiveness of the DAF approach. The clock extraction is achieved by using a half-bit-delay DAF ($\tau = 1/(2f_c) = T/2$). The computer simulation results are shown in Fig. 2.7 (optical spectrum) and Fig. 2.8 (RF spectrum). In Fig. 2.7, the dark and gray lines show the received optical spectrum of an RZ50 signal with and without a DAF filtering, respectively, when DL=10 ps/nm. Fig. 2.8(a) (zero dispersion) and Fig. 2.8(b) (10 ps/nm dispersion) further illustrate the difference of the detected RF spectra with and without DAF filtering. We can see that when there is no DAF filtering, shown in gray-colored curves, the clock frequency power was faded by only about 0.3 dB when the dispersion value is increased to 10 ps/nm. When there is DAF filtering, shown in dark curves, the clock component disappears when there is zero residual dispersion, and its power increases dramatically when the dispersion is increased to 10 ps/nm.

2.4 Effects of Bit Pattern, Modulation Formats, Finite MZI Extinction Ratio, and SPM

The amplitude of a clock component after a dispersive fiber link and a DAF depends not only on the accumulated dispersion of the transmission line, but also on the pulse shape and bit pattern of the transmitted data. The broadening or compression of a pulse width depends on whether the pulse propagates in an anomalous dispersion regime ($\beta_2 < 0$) or in a normal dispersion regime ($\beta_2 > 0$), and depends on the chirp parameter of the optical transmitted signals. Fig. 2.9(a) and Fig. 2.9(b) show the received pulse waveforms of a 40-Gb/s RZ50 signal for three different amounts of accumulated dispersions, without and with DAF filtering, respectively. An RZ50 signal is transmitted via two MZ modulators (functioning as data and pulse generators, respectively), both with an extinction ratio of 40 dB, and received with a 3rd -order Bessel lowpass filter (having a 60 GHz cutoff frequency) after a photo-detector. It is interesting to see that when the chromatic dispersion is increased, the clock frequency components appear on top of the marks ("1s"), and thus the clock component becomes very clear especially for the consecutive marks. Therefore, the amplitude of the clock frequency components is pattern-dependent, as will be discussed next.

To evaluate the impact of bit patterns, we conducted more computer simulations for 40-Gb/s RZ50 with three different patterns. The three patterns are (a) all marks, (b) alternate marks and spaces, i.e., 010101…, and (c) 512-bit pseudorandom binary sequence (PRBS) with equal probable marks and spaces using 50 different seeds. The extinction ratio of the MZ modulators (data and pulse generators) was set to be 40 dB in the simulation. Fig. 2.10 shows the clock power variation as a function of the accumulated dispersion and bit patterns for an RZ50 passing through a DAF. As already observed in Fig. 2.9, we can again see in Fig. 2.10 that the highest and lowest clock power occur when a bit pattern is composed of all marks and "0101" sequence, respectively. The detected clock power of PRBS with 50 different seeds is between those two cases. Moreover, we note that the clock power is zero not only at zero dispersion, but also at an accumulated dispersion of $N\times$77.8 ps/nm (N=1,2,3, …, etc.). This periodic phenomenon can be understood from the $cos(\theta_+ + 2qf_cf)$ term in (2–29): $I(f_c)$ equals to zero when $2qf_cf = \pi$ ($DL \cong$77.8 ps/nm when f_o = 193.3 THz, f_c = 40 GHz, $f = f_c/2$). Despite the fact that the clock power varies under different pulse shapes and bit patterns, it can still be used as a measure of the amount of residual dispersion in our proposed DAF method.

In this Section, we will also show that the proposed technique can work well even when fiber chromatic dispersion interacts with optical frequency chirp, which is caused by a finite DC extinction ratio of an MZ modulator or self-phase modulation (SPM). We will also show the system effects of different pulse shapes (via (2–29)) using five modulation formats including NRZ, RZ50, CS-RZ, RZ-DPSK, and CSRZ-DPSK.

Computer simulations are conducted at a line rate of 40 Gb/s using MZ-modulator-based data and pulse generators, both with an extinction ratio of 40 dB, and the dependence of clock power (after a DAF) on accumulated dispersion is shown in Fig. 2.11. All transmission parameters are the same as those used in Fig. 2.6. Two values of $\delta\tau/\tau_0$ (0 and 6.25%) are used. We can see that the clock power for all five modulation formats becomes zero when there is zero accumulated dispersion at a zero delay variation. When $\delta\tau/\tau_0 \leq 6.25\%$, the dynamic range of the clock power around zero dispersion is ≥ 8 dB for all modulation formats. Here the dynamic range is defined as the variation range of the detected clock power within the monitoring window. This minimum dynamic range in combination with a dispersion monitoring window of ~±30 ps/nm (slightly smaller than that of the AM pilot-tone + DAF based method discussed in Section 2.2) for all modulation formats result in a minimum dispersion resolution of (30ps/nm)/(8 dB)= 3.75 ps/nm/dB, which is quite sufficient for the VDC in Fig. 2.3 to reduce the total dispersion close to zero. Note that CS-RZ always has the worst dynamic range around zero dispersion while $\delta\tau/\tau_0 \neq 0$, because the neighbor CS-RZ optical pulses have a phase difference of π which results in an amplitude-cancellation effect.

Four clock power detection methods for dispersion equalization are compared in Fig. 2.12. The four methods are

(1) direct detection of the clock power;

(2) direct detection of the half-clock power;

(3) direct detection of the clock power with a half-bit-delay in DAF;

(4) direct detection of the half-clock power with a one-bit-delay in DAF.

We summarize the results of dispersion resolution around zero dispersion and monitoring window in Table 2.1. The “high” dispersion resolution in Table 2.1 is defined as $\Delta P > 6$ dB within a residual dispersion window of ±30 ps/nm. Note that because the residual dispersion is always controlled to be within ±30 ps/nm, the dispersion penalty for all 40 Gb/s modulation formats under consideration is less than

1 dB. We see that method (3) enables high dispersion resolution for all five modulation formats, while maintaining a relatively high monitoring window (>56 ps/nm). By lowering the detected clock power frequency by 50% in method (4), a greater than 4 times monitoring window of 300 ps/nm (i.e., ±150 ps/nm) can be achieved. However, most modulation formats can no longer have a good dispersion resolution, except for NRZ. For RZ50 and CS-RZ signal formats, one can combine methods (3) and (4) to achieve both a high dispersion resolution and a large monitoring window. For RZ-DPSK, the most cost-effective solution is to combine methods (2) and (3). For CSRZ-DPSK, the direct half-clock power detection is the best choice, and the DAF method is not needed.

Residual frequency chirp due to a finite modulator DC extinction or SPM is studied next, while a half-bit-delay DAF clock detection technique is used. We use the eye opening penalty (EOP) to evaluate a system performance, whereas EOP is defined as [15]

$$EOP(dB) = 10\log_{10}\left(\frac{\text{Eye opening back to back}}{\text{Eye opening after transmission}}\right) \qquad (2\text{–}30)$$

An EOP of 0.5 dB and 1 dB represents 90% and 80% eye opening, respectively. In addition, an EOP is estimated using a receiver whose bandwidth is 0.7 times of the data rate. All waveforms were simulated without considering optical amplified noise. We assume a modulator is driven by a 40-Gb/s RZ50 signal with a random word length of 2^9, which corresponds to a frequency resolution of ~78MHz (40e9/512). All simulation parameters are the same as those in Fig. 2.6. Fig. 2.13(a) shows the EOP of an RZ50 signal as a function of residual dispersion with various MZ modulators (both data and pulse generators) DC extinction ratios (20 and 40 dB). We see that the lower the MZ modulator extinction ratio, the more asymmetric is the dispersion penalty curve with respect to zero dispersion. This is because an MZ modulator with a finite DC extinction ratio will always be accompanied by a residual chirp [16],[17], which implies that the phase of e-field has an initial frequency chirp term, in addition to the link distance-dependent chromatic dispersion phase term (proportional to $DL\,f_c^2$). As a result, zero clock power occurs when the initial frequency chirp-induced phase term is cancelled by a small amount of residual dispersion-induced phase term, and therefore zero clock power occurs at a non-zero residual dispersion value, as shown in Fig. 2.13(b). We can see that the minimum clock power occurs at the minimum-EOP residual dispersion, and not at a zero residual dispersion.

Residual frequency chirp could also be generated by SPM [18]. The MZ modulators with extinction ratio of 40 dB are used in the simulation, and the transmission parameters are the same as those used in Fig. 2.6, except that we purposely increase the fiber launched power to 12 dBm/ch. Fig. 2.14 shows the EOP (a) and clock power (b) of an RZ50 signal with a launched power of −3 and 12 dBm/ch, respectively. We can see that at a 12 dBm/ch launched power, the minimum EOP and clock power occur at ~2 ps/nm instead of 0 ps/nm residual dispersion. The minimum EOP at 12 dBm/ch is only about 1 dB higher than that at −3 dBm/ch.

2.5 Experimental Results

To demonstrate the feasibility of the proposed dispersion monitoring technique, we performed an experiment using a half-bit-delay DAF filter for RZ signal. In addition, the result of one-bit-delay DAF filter has been demonstrated and reported recently [20].

We conducted the experiment of a 10.61 Gb/s RZ system. An RZ transmitter consists of a tunable continuous-wave (CW) laser with a linewidth of 100 kHz, an electro-absorption modulator (EAM) for pulse carving, and an intensity modulator. The CW light was carved into a pulse train with a pulse-width of 28 ps via an EAM, which was driven by a 10.61 GHz sinusoidal clock signal. The pulse train was then intensity-modulated by a 10.61 Gb/s NRZ pseudorandom binary sequence of pattern length 2^{31}-1 using a $LiNbO_3$ modulator. After photo-detection and amplification, the clock frequency power as a function of the accumulated dispersion is shown in Fig. 2.15 with and without using a half-bit-delay DAF, respectively. With half-bit-delay DAF filtering, the detected clock power is minimum at zero accumulated dispersion, and the monitoring window of ~±640 ps/nm was obtained here for a 10.61 Gb/s RZ transmitter. It is equivalent to the monitoring window of ~±40 ps/nm in a 40 Gb/s RZ transmitter, because the fiber dispersion-induced phase shift is proportional to square of bit rate.

In [20], a 10 Gb/s NRZ signal and an DAF with differential delay of one-bit delay were used, and the monitoring window of > ±2300 ps/nm was obtained by half clock frequency detection. This monitoring window is equivalent to >~±143.8 ps/nm (2300/16≅143.8) for 40 Gb/s system, while our simulation result is ±150 ps/nm shown in Table 2.1. Fig. 2.16 shows the experimental setup reported in [20]. A 10 Gb/s NRZ signal with PRBS pattern length of 2^{23}–1 is transmitted through dispersive link, which consists of a section of single-mode fiber and fiber-based dispersion compensation modules. After propagating through dispersive link, a portion of optical signal is tapped off and sent to dispersion measurement system. The signal is first amplified by an optical amplifier, because the measured RF power depends on the received optical power. The signal then passes through a fiber-based DAF with differential delay of 100 ps (one-bit delay). The DAF is maintained at quadrature by adjusting the temperature of one arm. The optical signal is converted to photocurrent by means of a photodiode with 20 GHz bandwidth. For each dispersive link test, the optical power into the photodiode is keep at 2.9 mW to ensure the

measured RF power variations result from accumulated dispersion changes, not from optical power fluctuations. The RF power at 5 GHz (half-clock frequency) is measured using an RF spectrum analyzer with resolution bandwidth of 1 MHz. The measured RF power at 5 GHz for various values of accumulated dispersion is shown in Fig. 2.17. The measurement result demonstrates the monitoring window of > ±2300 ps/nm and a good agreement with the theory.

Campillo [20] also mentioned that the monitoring window can increase further by increasing the value of differential delay of a DAF. A path length difference of 250 ps will produce a monitoring window of more than ±15000 ps/nm for 10 Gb/s NRZ signals (equivalent to more than ~±938 ps/nm for 40 Gb/s NRZ signals), while RF power at 2 GHz is detected. Note that much smaller frequencies may cause problems, in case the laser linewidth has to be broadened to increase SBS threshold. Moreover, to maintain biasing at DAF quadrature becomes more difficult, because increased DAF differential delay will lead to temperature-dependent variations.

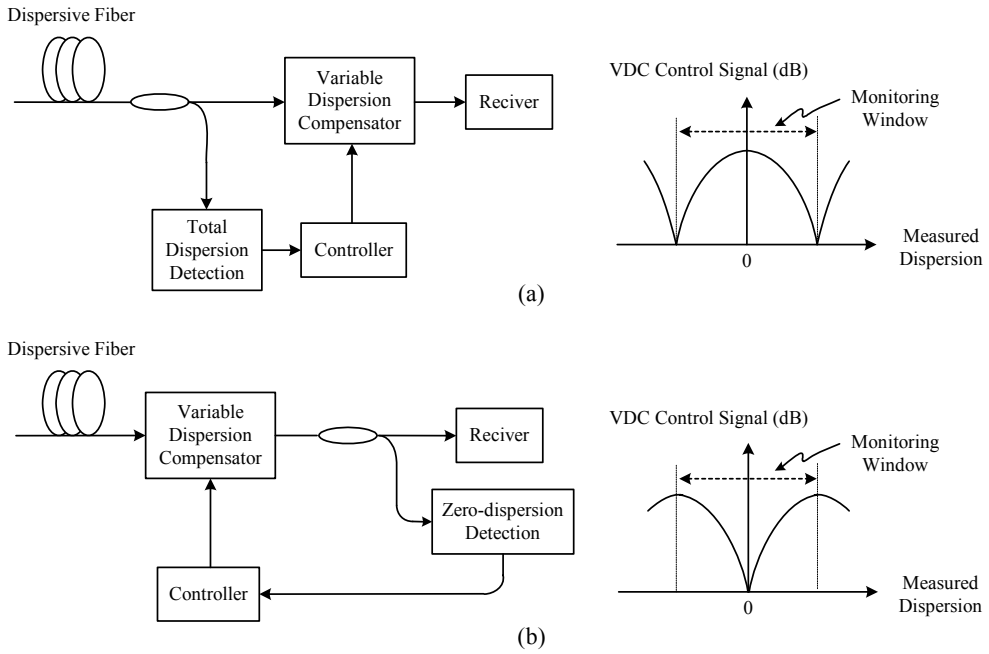

Fig. 2.1 Pre-detection (a) and post-detection (b) configurations for a complete dispersion equalization setup.

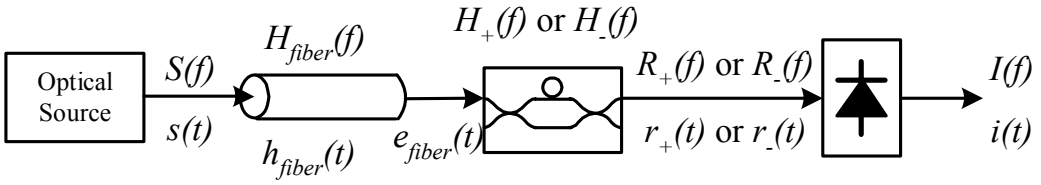

Fig. 2.2 A simplified block diagram of an optical transmission system with a DAF.

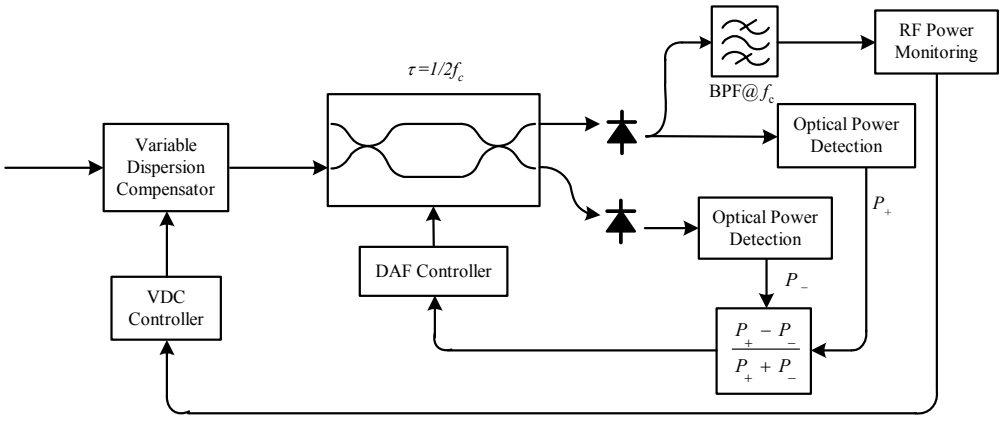

Fig. 2.3 A complete adaptive dispersion equalizer which is composed of a VDC and the proposed post-detection dispersion monitoring technique. A DAF controller is used to adjust the delay τ to ensure that f_o is aligned with a DAF quadrature point. The VDC is controlled by the monitored clock or pilot-tone RF power, which should be minimized by the VDC.

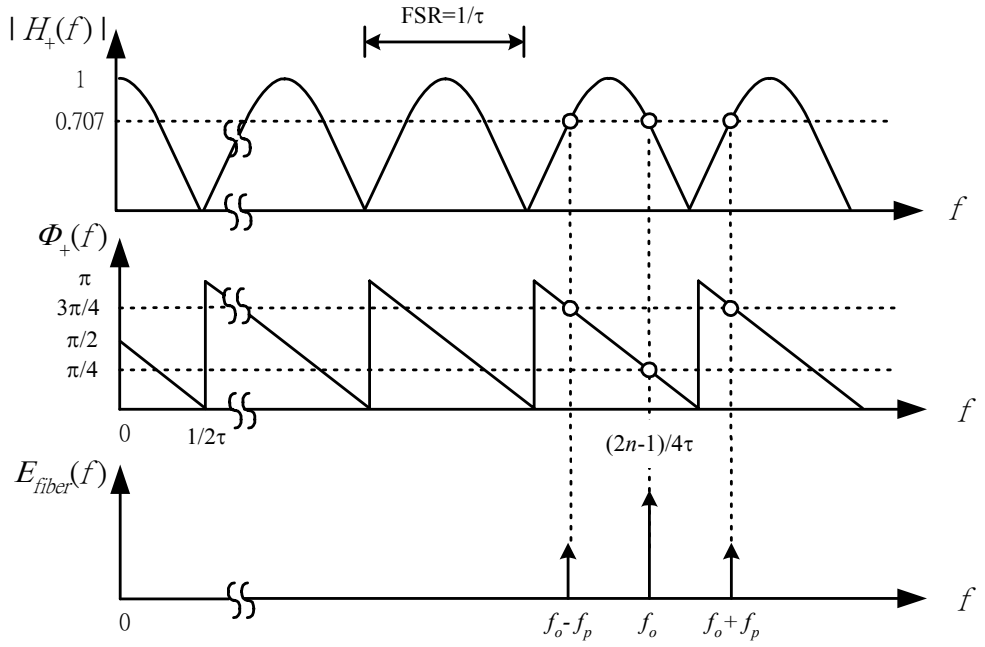

Fig. 2.4 Optical amplitude (a) and phase (b) responses of a DAF at its constructive port. Also shown is the electric field spectrum consisting of an optical carrier and its associated pilot tones.

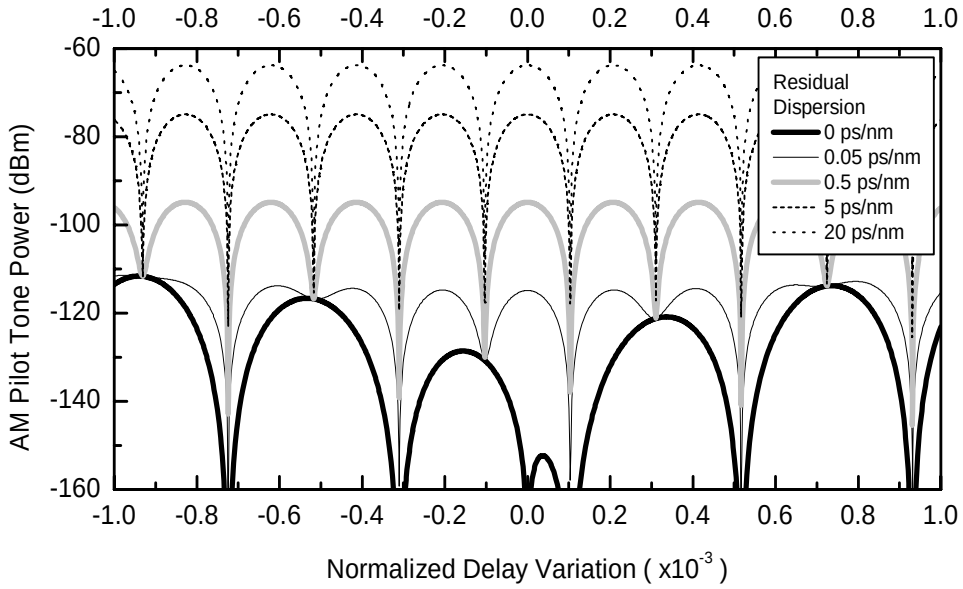

Fig. 2.5 Power fading effect of an AM pilot tone @ 40 GHz due to differential optical delay variation under five accumulated fiber dispersions. The optical wavelength is 193.3THz (~1552.0 nm) which satisfies Eq. (2−3).

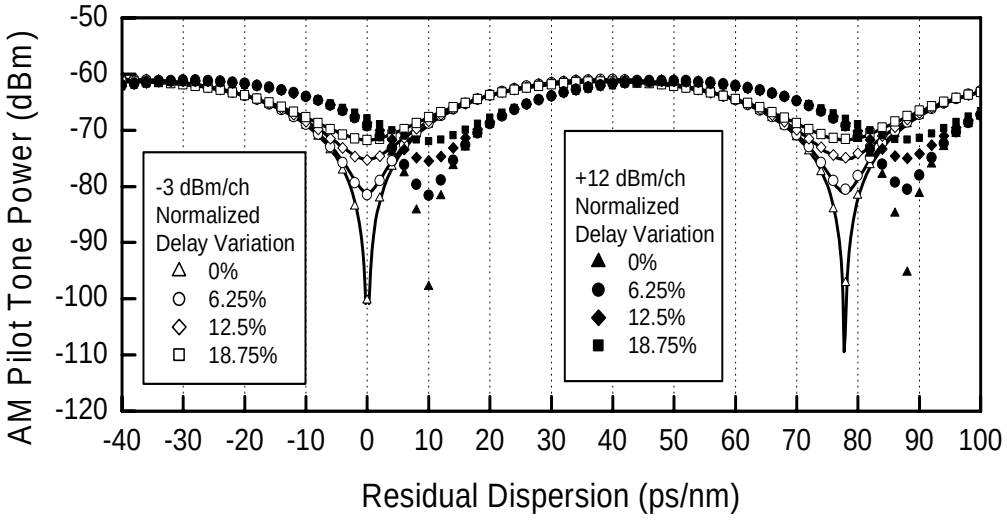

Fig. 2.6 Calculated (solid-lines) and simulated (symbols) AM pilot tone power as a function of accumulated dispersion with various differential optical delays in solid curves. The optical carrier is at the quadrature point of the power transfer function of the DAF. Simulation parameters are: sampling frequency=1.28 THz, f_p=40 GHz, data length=512 bits, fiber launched power= −3 dBm/ch and 12 dBm/ch, fiber length (SMF)=50 km, fiber loss=0.2 dB/km, D=16 ps/nm/km, dispersion slope=0.08 ps/nm^2/km, fiber nonlinear coefficient=1.32 W^{-1}km^{-1}, transmitter MZ modulator extinction ratio=40 dB. $\delta\tau/\tau_0$={0%, 6.25%, 12.5%, 18.75%}, i.e. τ={1/2/40e9, 1/2/42.6667e9, 1/2/45.7143e9, 1/2/49.2308e9}; and f_o={193.28e12 + 40e9/2, 193.28e12 + 42.6667e9/2, 193.28e12 + 45.7143e9/2, 193.28e12 + 49.2308e9/2 } Hz. The choices of f_o are to satisfy condition (2) (Eq.(2−3)) described in Section 2.2.

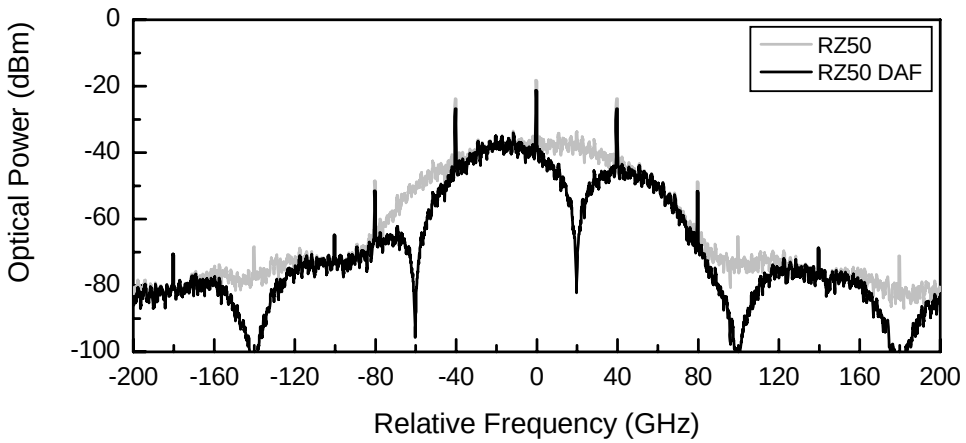

Fig. 2.7 Simulated optical spectrum of RZ50 signal without (gray lines) and with (black lines) DAF filtering. The display resolution bandwidth is 625 MHz. Simulation parameters are the same as those in Fig. 2.6. $\delta\tau/\tau_0=0$.

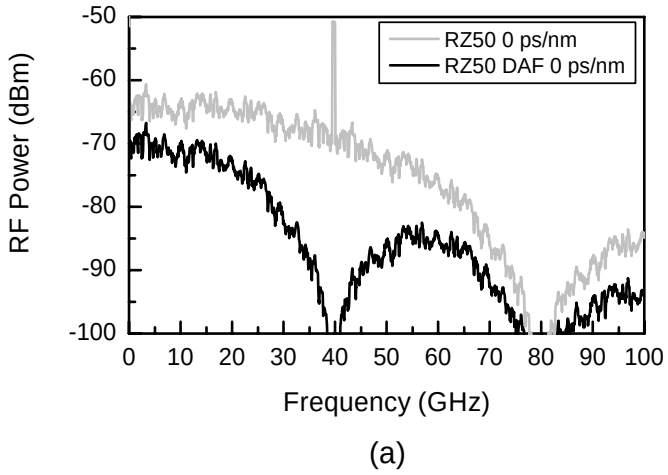

(a)

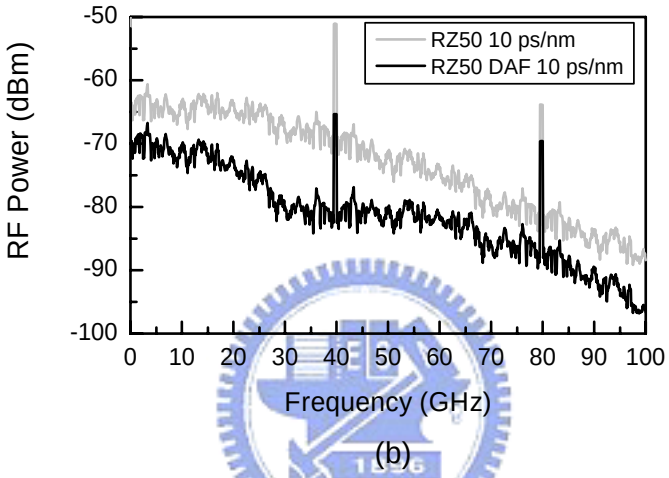

(b)

Fig. 2.8 Simulated RF spectrum of received (a) RZ50 signals under 0 ps/nm dispersion and (b) RZ50 signals under 10 ps/nm dispersion without (gray lines) and with (black lines) DAF filtering, respectively. The display resolution bandwidth is 625 MHz. Simulation parameters are the same as those in Fig. 2.6. $\delta\tau/\tau_0=0$.

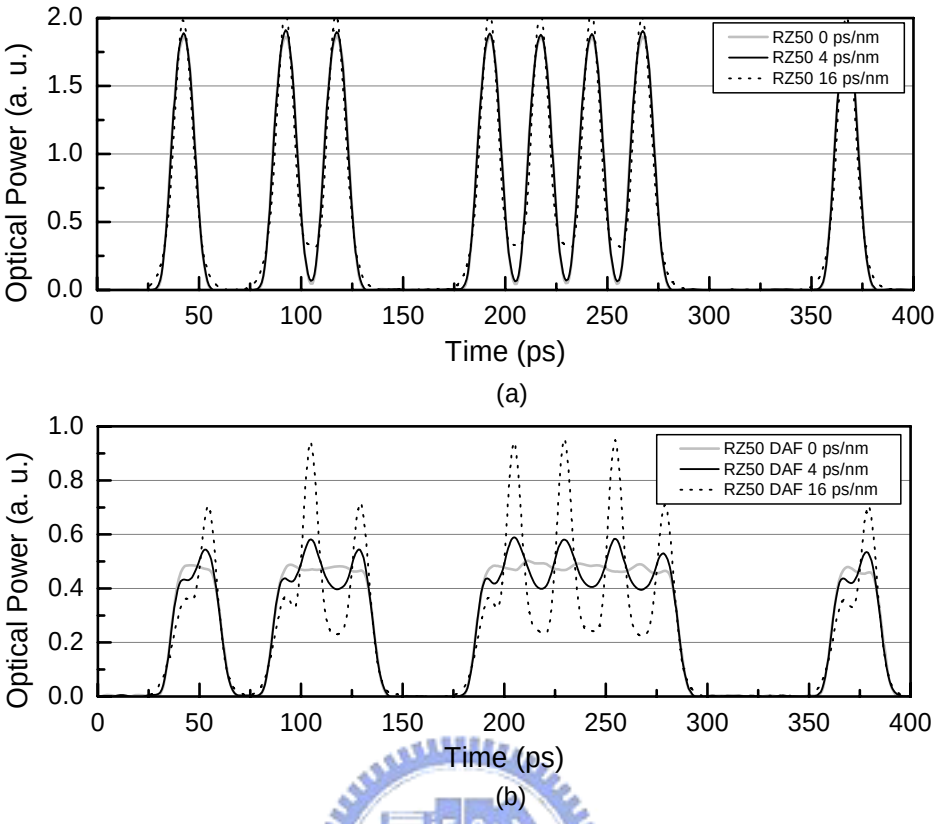

Fig. 2.9 Simulated pulse waveforms of 40-Gb/s RZ50 signals under three different amounts of accumulated dispersion (0, 4, and 16 ps/nm), without (a) and with (b) DAF filtering. Simulation parameters are the same as those in Fig. 2.6. $\delta\tau/\tau_0$=0. The cutoff frequency of a 3rd-order Bessel LPF (after photo-detection) is 60 GHz.

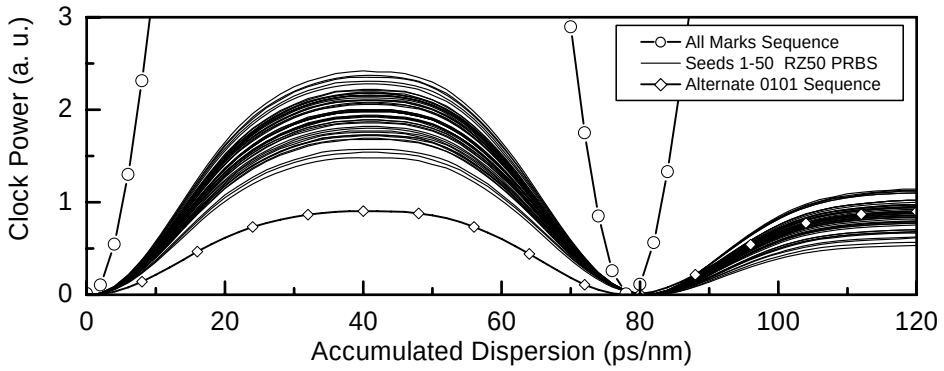

Fig. 2.10 Simulated clock power after DAF filtering as a function of accumulated dispersion for 40-Gb/s RZ50 with different bit patterns. Clock power was detected through a bandpass filter @ 40 GHz with a bandwidth of 100 MHz. Simulation parameters are the same as those in Fig. 2.6. $\delta\tau/\tau_0=0$. PRBS uses 50 different seeds.

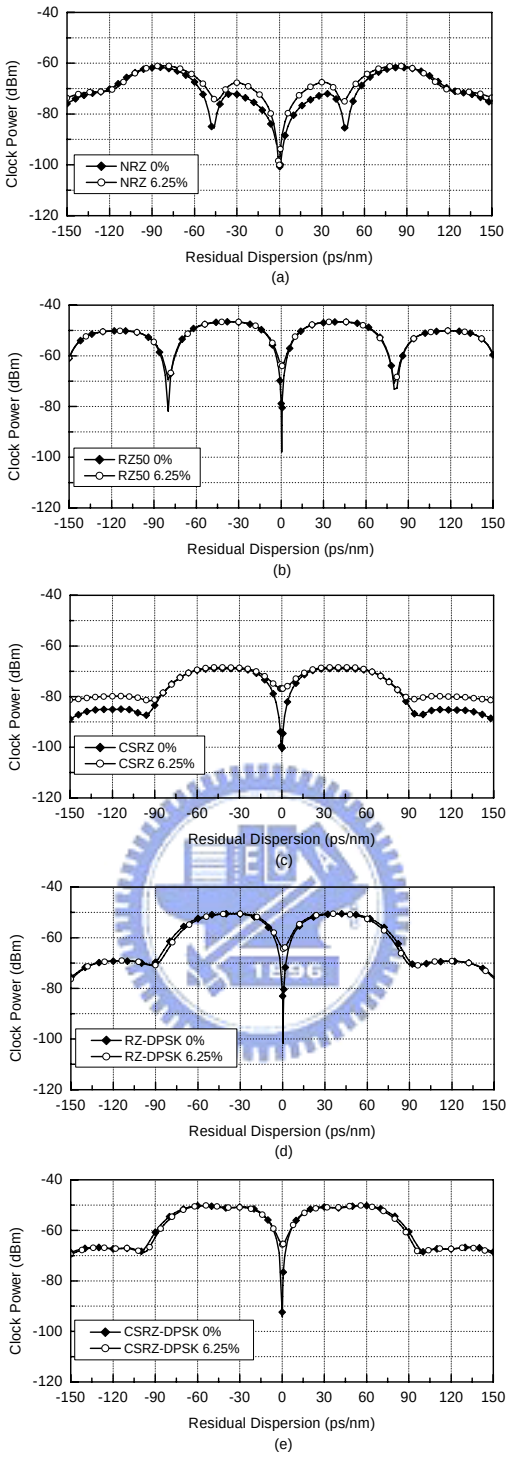

Fig. 2.11 Clock power after DAF filtering as a function of residual dispersion, with a DAF normalized delay variation of 0% and 6.25%, respectively, for 40-Gb/s (a) NRZ, (b) RZ50, (c) CS-RZ, (d) RZ-DPSK and (e) CSRZ-DPSK. All simulation parameters are the same as those in Fig. 2.6. f_o={193.28e12 + 40e9/2, 193.28e12 + 42.6667e9/2} Hz for $\delta\tau/\tau_0 = 0$ and 6.25%, respectively, which implies that f_o is always aligned with a DAF quadrature point. RF power was detected through a BPF@40GHz with a 500 MHz bandwidth.

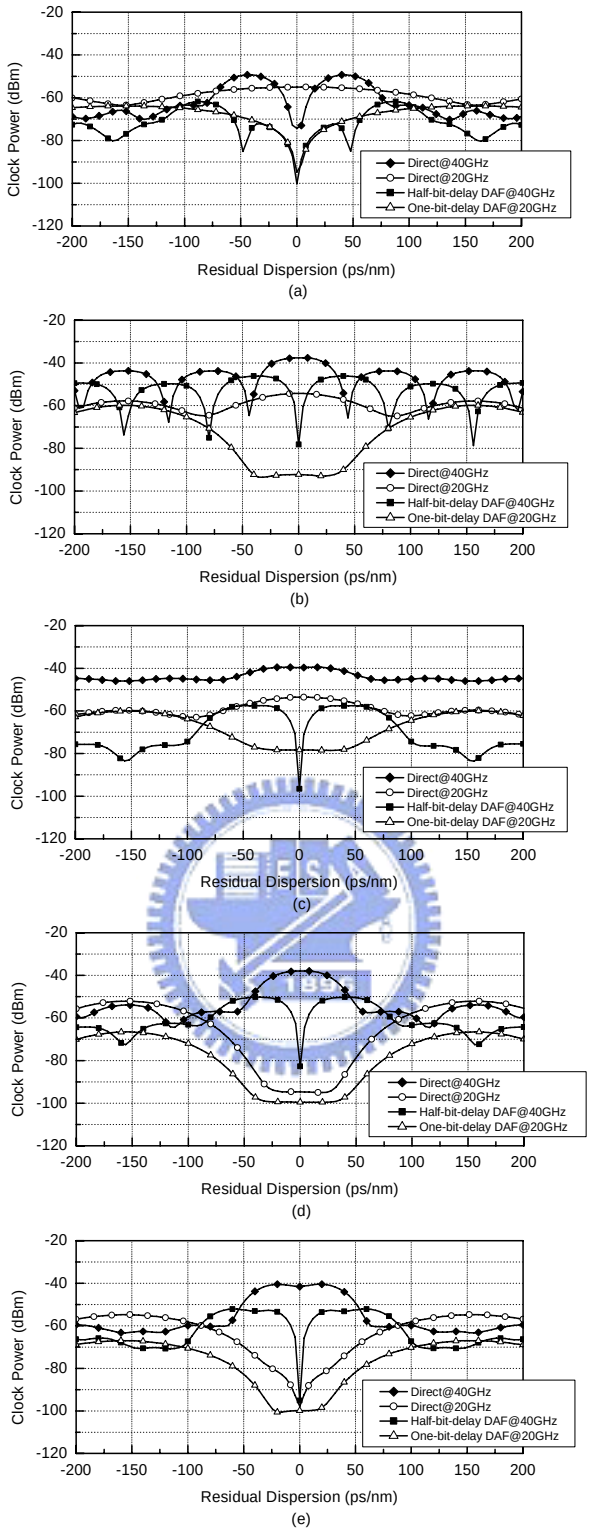

Fig. 2.12 Clock and half-clock power with and without DAF filtering as a function of residual dispersion, for 40-Gb/s (a) NRZ, (b) RZ50, (c) CS-RZ, (d) RZ-DPSK and (e) CSRZ-DPSK. All simulation parameters are the same as those in Fig. 2.6. RF power was detected through a BPF at 20 and 40GHz, respectively, with a 500 MHz bandwidth.

Table 2.1 Comparison of dispersion resolution around zero dispersion and dispersion monitoring window of 5 modulation formats for four power detection methods at 40 Gb/s. Note that “high” dispersion resolution is defined as when ΔP/ΔDL > 6 dB.

		NRZ	RZ50	CS-RZ	RZ-DPSK	CSRZ-DPSK
Direct detection @clock	ΔP/ΔDL	High	Low	Low	Low	
	Monitoring Window	± 40 ps/nm	± 40 ps/nm	± 70 ps/nm	± 50 ps/nm	
Direct detection @half clock	ΔP/ΔDL	Low	Low	Low	Low	High
	Monitoring Window	±150 ps/nm	± 75 ps/nm	± 90 ps/nm	±150 ps/nm	±150 ps/nm
Half-bit-delay (12.5 ps) DAF @clock (40 GHz)	ΔP/ΔDL	High	High	High	High	High
	Monitoring Window	± 34 ps/nm	± 36 ps/nm	± 34 ps/nm	± 34 ps/nm	± 28 ps/nm
One-bit-delay (25 ps) DAF @half clock (20GHz)	ΔP/ΔDL	High	Low	Low	Low	Low
	Monitoring Window	±150 ps/nm	±150 ps/nm	±150 ps/nm	±150 ps/nm	±150 ps/nm

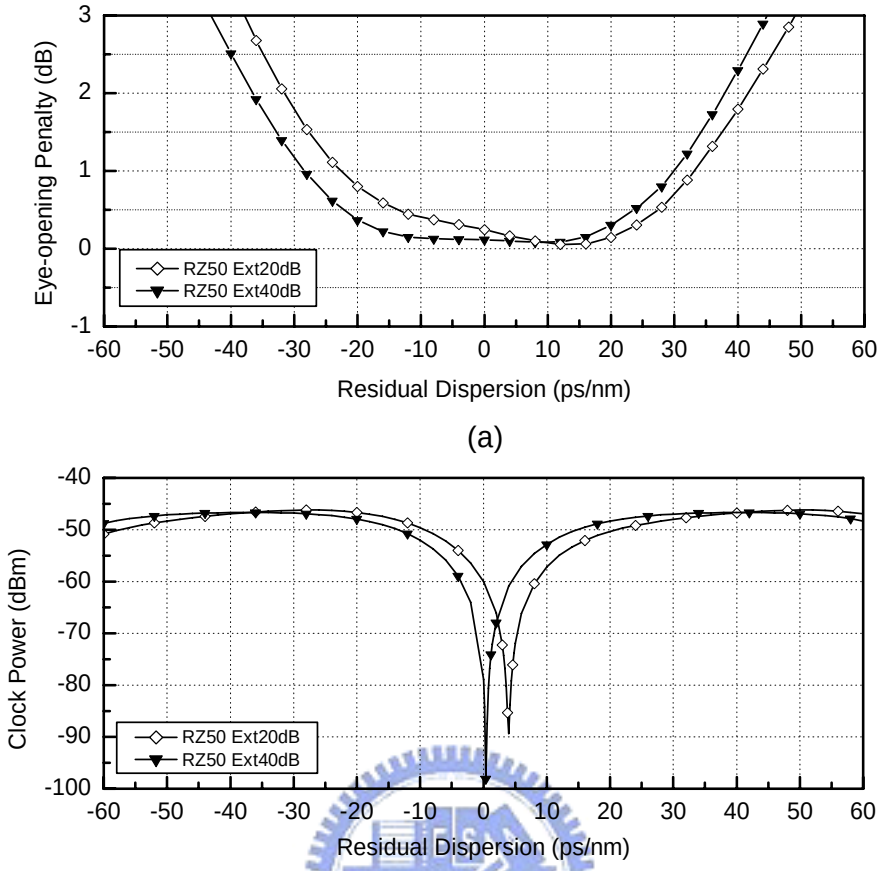

Fig. 2.13 Simulated EOP (a) and the corresponding clock power (b) as a function of residual dispersion with finite MZ modulator DC extinction ratios, 20 (open diamond) and 40 dB (down triangle), respectively, for a 40-Gb/s RZ50 signal. Simulation parameters are the same as those in Fig. 2.6. $\delta\tau/\tau_0=0$. RF power was detected through a BPF@40GHz with a 500 MHz bandwidth.

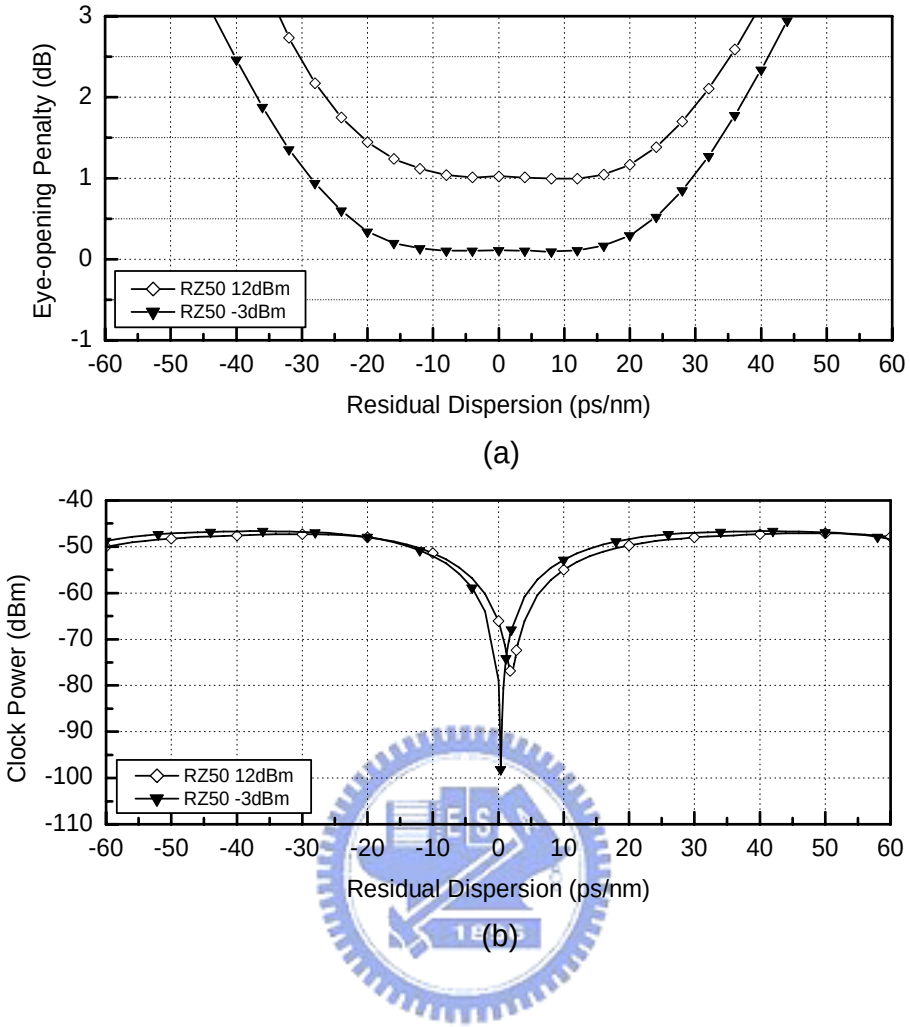

Fig. 2.14 Simulated EOP (a) and the corresponding clock power (b) as a function of residual dispersion with fiber launched power of -3 (triangle) and 12 dBm/ch (open diamond), respectively, for a 40-Gb/s RZ50 signal. Simulation parameters are the same as those in Fig. 2.6. $\delta\tau/\tau_0=0$. RF power was detected through a BPF@40GHz with a 500 MHz bandwidth.

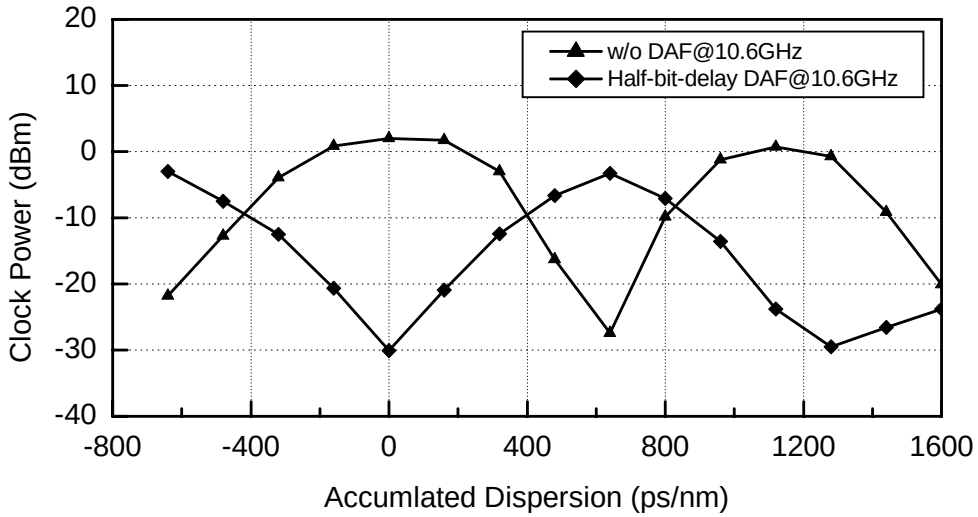

Fig. 2.15 The power at clock frequency of 10.61 GHz as a function of the accumulated dispersion with and without using a half-bit-delay DAF, respectively. An 10.61 Gb/s RZ transmitter with a pulse-width of 28 ps was used in the experiment

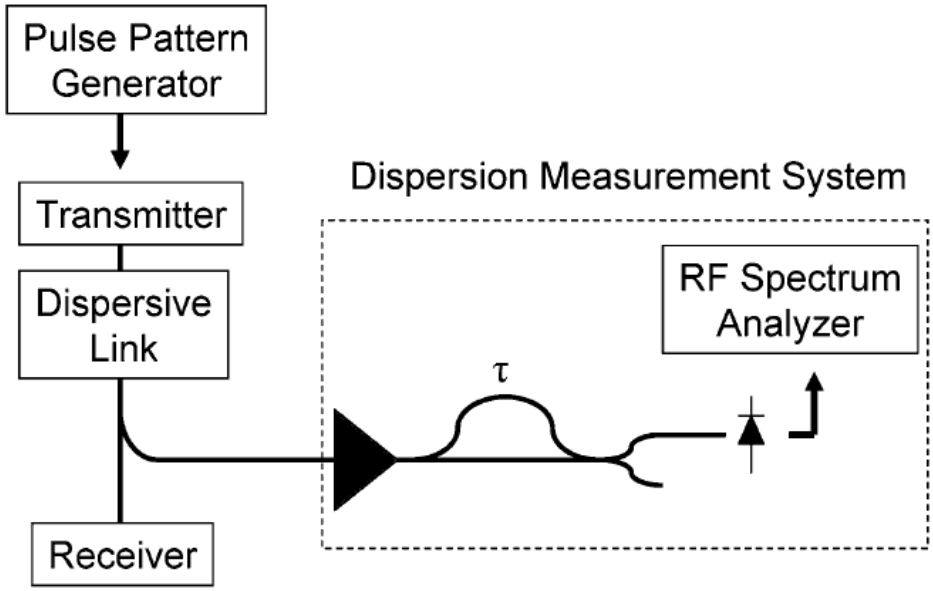

Fig. 2.16 Experimental setup [20]. A 10 Gb/s pseudorandom signal is transmitted through dispersive link. A portion of received signal is amplified, and passed through a DAF with differential delay of 100 ps (one-bit delay), and detected by a photodiode. The RF power at 5 GHz (half-clock frequency) is measured by an RF spectrum analyzer.

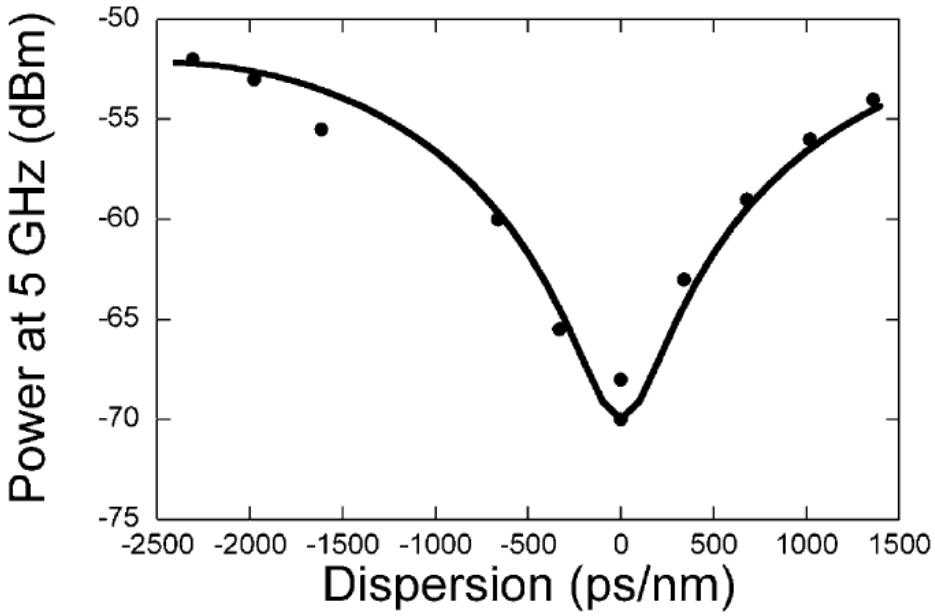

Fig. 2.17 Received RF power at 5 GHz (half-clock frequency) as a function of accumulated dispersion for 3-mA DC current on the photodiode. The solid line is a calculation fit [20].

Chapter 3 Pulse-Carver and Data Alignment Monitoring

3.1 Introduction

In an RZ-DPSK system, the correct timing between pulse carving and phase modulation must be maintained. This has recently been recognized as a challenging task, because of the unavoidable optical/electronic device aging and the temperature variation-induced optical length change between the two modulators [21-23]. For example, it was reported that a 10 Gb/s RZ-DPSK system power penalty increases rapidly when the timing alignment exceeds 15 ps [22]. This is equivalent to 3.75 ps in a 40 Gbps RZ-DPSK system, which can be easily incurred due to temperature variations [21]. Therefore, an automatic alignment method is needed for a long-term stable field deployment. Two methods have so far been published for this purpose [21], [22]. The first method measured the degree of polarization (DOP) change due to timing-misalignment by using a polarization-maintaining-fiber, a polarizer, and an optical power meter. A very limited monitored power dynamic range of ~0.2 dB was obtained. The second method [22] used an off-center optical filter to capture the frequency chirp induced by the timing-alignment, but the monitored DC power dynamic range is limited to only 3.35 dB for a 10.61 Gb/s RZ-DPSK.

In this Chapter, we use an optical frequency discriminator and a microwave detector centered at a half of the phase modulation data rate to monitor the misaligned timing. This timing-misalignment detection method can be used when the phase modulation is implemented by either a dual-arm Mach-Zehnder (MZ) modulator or a phase modulator. Compared with previous monitoring schemes [21-23], this polarization-independent method can achieve a much larger dynamic range of ~17.5 dB, and therefore a much higher monitoring sensitivity.

3.2 Conventional Techniques

In this section, we will briefly summarize the two reported methods that were developed to align the timing between pulse carver and phase modulator.

3.2.1 DOP Method [21]

As shown in Fig. 3.1, a scheme to monitor the alignment status of RZ-DPSK is proposed by measuring the power variation after polarizer, which is induced by the reduction of signal's DOP due to the timing-misalignment after propagation in an intentionally introduced finite differential group delay.

However, the monitoring power dynamic range (MPDR) of ~0.2 dB is achieved within the timing alignment range of half-bit period by this method, so measurement error might be incurred under polarization fluctuation of the incoming signal.

3.2.2 Off-center Filtering Method [22]

An off-center optical filter is employed to capture the chirp induced by misalignment. As shown in Fig. 3.2, a portion of RZ-DPSK transmitter output is tapped off and fed into alignment-monitoring module, which only consists of optical bandpass filter (BPF) and an optical power meter. The optical filter is adjusted to be offset from the signal center wavelength, and the output optical power of the optical BPF is used as a monitoring signal for timing alignment.

By filtering out a narrow slice from the edge of the signal spectrum, any misalignment-induced spectrum broadening will be translated into an increased output power from the optical filter. However, as there are periodic power nulls in the signal spectrum, if the filter bandwidth is smaller than the null spacing, the monitoring power change will fluctuate with respect to filter center frequency. The filter bandwidth and signal occupied spectrum will make the monitoring more sensitivity to the filter center frequency stability, and therefore the filter center frequency should be chosen to give the maximum MPDR. The optical filter with bandwidth of 0.22 nm and frequency offset of 0.5 nm are used in 10.61 Gb/s RZ-DPSK system, and the MPDR of 3.35 dB was reported.

3.3 Operation Principle of Proposed Alignment Monitoring Technique for RZ-DPSK Systems

The proposed configuration is shown in Fig. 3.3(a). A small portion of the transmitted optical signal is tapped and passed through an optical frequency discriminator. After photo-detection, RF bandpass filtering and envelope detection, the output is fed into a control circuit which drives a voltage-controlled phase shifter to adjust the time delay between the data and clock signal. The phase shifter is adjusted until a minimum of detected microwave power is reached. Note that if the optical frequency discriminator is temperature stabilized, it could serve as a wavelength locker.

In order to obtain a clear idea about how an optical frequency discriminator functions and what the important design parameters are, we provide a closed-form analysis in this section. We first assume that the optical field of a modulated light source to be

$$e(t) = \sqrt{i(t)}\ e^{j[\Omega t + \phi(t)]} \tag{3–1}$$

where $i(t)$ and $\phi(t)$ are the intensity and phase modulations, respectively, and Ω is the angular frequency of optical carrier. For an RZ-DPSK signal, $\phi(t) = \sum_{n=-\infty}^{\infty} \pi I_n m(t - nT)$, where $\{I_n\}=\{0, 1\}$ is data sequence with equal probability, and $m(t)$ is the phase modulator driving pulse in one bit slot. Also, $i(t)$ is an RZ pulse train given by $\sqrt{i(t)} = \sum_{k=-\infty}^{\infty} s(t - kT - t_o)$, where $s(t)$ is an optical pulse within an interval of $[-0.5T, 0.5T]$, T is the bit duration, and t_o represents the misalignment ($-0.5T \le t_o \le 0.5T$). The frequency chirp caused by the phase modulation can be written as

$$\delta\nu(t) = \frac{1}{2\pi}\frac{d}{dt}\phi(t) \approx \frac{1}{2\pi}\frac{\phi(t) - \phi(t-\tau)}{\tau} = \frac{\Delta\phi(t,\tau)}{2\pi\tau} \tag{3–2}$$

where $\Delta\phi(t,\tau) = \phi(t) - \phi(t-\tau)$ and τ is sufficiently small. In the followings, we will see that $\Delta\phi(t,\tau)$ can be obtained directly from an analysis based on a delay-and-add frequency discriminator, given that $\Delta\phi(t,\tau)$ is also sufficiently small. This closed-form analysis can help us gain a clear physical insight of the proposed

method even though the physical optical frequency discriminator may not be a delay-and-add filter.

After passing $e(t)$ through a delay-and-add optical frequency discriminator operating at a quadrature point, we can obtain the detected photo-current as

$$P(t) = i(t) + i(t-\tau) \pm 2\sqrt{i(t)\,i(t-\tau)}\sin\left[\Delta\phi(t,\tau)\right] \qquad (3\text{–}3)$$

where ± represents the data captured at the positive or negative slope of the optical frequency discriminator. In (3–3), the first two terms are the RZ pulse train and its delayed replica. The third term is the product of the intensity modulation and the frequency chirping, and is directly proportional to $\Delta\phi(t,\tau)$ when $|\Delta\phi(t,\tau)| << 1$. We can see that this interference term exists only when the RZ pulse amplitude and the frequency chirp are both non-zero. Fig. 3.4 shows that although frequency chirp always occurs during data transitions (Fig. 3.4(b)), the interference term exists only when the RZ pulses are misaligned with respect to the modulating data, as shown in Fig. 3.4(d). In other words, only when a part of the carved RZ pulse enters the data transient region due to timing misalignment, can the frequency chirp be observed and measured. Note also that the first and second terms in (3–3) are not dependent on the timing misalignment, and their presence in a measured result could decrease the monitoring dynamic range at DC and the clock frequency. Therefore, our measurement focuses on the third term to improve the dynamic range in [22]. Besides RZ-DPSK, this method can also be applied to other modulation techniques such as RZ and CS-RZ, which use two optical modulators for data and clock, respectively.

The RF power spectrum of the detected photo-current can be obtained by taking the Fourier transform of the autocorrelation function of (3–3). It is composed of the power spectrum of the RZ pulse train, which has spikes occur at the clock frequency and its harmonics, and the power spectrum of the interference term given by

$$P_{\text{int}}(f, t_o, \alpha, \tau) \propto \left[s^2\left(0.5T - |t_o|\right) \frac{\sin(\pi T f)\cos(\alpha\pi T f)}{1-(2\alpha T f)^2}\tau \right]^2 \qquad (3\text{–}4)$$

where we have assumed that the phase modulating data $m(t)$ has a raised cosine pulse shape with a roll-off factor α. We can see that the RF spectrum level is proportional

to the misaligned pulse shape $s(0.5T-|t_o|)$ and the differential delay τ. When t_o=0, P_{int} is zero because $s(0.5T)$=0. For a fixed non-zero t_o, the power spectral density of the interference term is zero at f =0 and f =1/T. The maximum power spectral density is around f =1/(2T) depending on roll-off factor α, as shown in Fig. 3.5. Note also that (3–4) has no power at f =1/T. Therefore, the highest detection sensitivity and dynamic range can be obtained if we use a narrowband microwave filter centered at 1/(2T). Theoretically, the dynamic range can reach infinity because the detected microwave power between totally-misaligned and perfectly-aligned timing is given by $[s(0)/s(0.5T)]^4$ where $s(0.5T)$ is zero. In practice, however, the dynamic range is limited by the microwave detector noise.

There exists a tradeoff to select a proper differential delay τ. The differential delay has to be small to ensure that the frequency excursion is within the linear slope of the frequency discriminator, as shown in Fig. 3.3(b), i.e., $[\delta\nu(t)]_{\text{pk-to-pk}} < \text{FSR}/2 = 1/(2\tau)$, where FSR is the free-spectral-range of the delay-and-add filter. On the other hand, according to (3–4), the longer the differential delay τ, the larger the power variations induced by the discriminator.

3.4 Experimental Results

3.4.1 Experimental Setup

An experiment was conducted to verify the feasibility of the proposed method in a 10.61 Gb/s RZ-DPSK system. An RZ-DPSK transmitter consists of a tunable continuous-wave (CW) laser with a linewidth of 100 kHz, an electro-absorption modulator (EAM) for pulse carving, and an optical phase modulator. The CW light was carved into a pulse train with a pulse-width of 28 ps via an EAM, which was driven by a 10.61 GHz sinusoidal clock signal. The pulse train was then phased-modulated by a 10.61 Gb/s NRZ pseudorandom binary sequence of pattern length 2^{31}-1 using a $LiNbO_3$ phase modulator. At the output of the RZ-DPSK transmitter, a portion of optical power was tapped off and fed into an optical thin-film filter-based optical frequency discriminator with a linear frequency transition range of ~0.3 nm. After photo-detection and electrical amplification, an RF spectrum analyzer was used to observe the RF power variations for different misalignment conditions. Different misalignment conditions were achieved by manually adjusting a tunable delay between the 10.61 GHz sinusoidal clock and the EAM. As for the direct detection of DPSK data signals, a single-ended Mach-Zehnder interferometer with a relative arm delay of 94 ps was used before a PIN photodiode.

3.4.2 Results and Discussions

Fig. 3.6(a) shows the phase modulator driving signal in our experiment, and Figs 3.6(b) and 3.6(c) show the detected RZ pulses using the optical frequency discriminator. Both Figs 3.6(b) and 3.6(c) were obtained when the CW laser frequency was aligned to the −3 dB point of the optical thin-film filter at its positive slope, at a timing misalignment of 0 and 47 ps, respectively. In Fig. 3.6(b), the AM signal (RZ pulse trains) with no FM-to-AM conversion component appeared at the output of the optical frequency discriminator. In Fig. 3.6(c), the largest possible clock misalignment, i.e. the half-bit misalignment, was selected to demonstrate an added FM-to-AM conversion component appeared at the rising edge of the driving signal (this is because we used the positive slope of the filter).

Fig. 3.7 shows the measured RF spectrum of a 10.61 Gb/s RZ-DPSK signal with a clock misalignment of 0, 26 and 47 ps, respectively. Again, the CW laser frequency is aligned to the −3 dB point of the optical filter at its positive slope. As

expected, the relative amplitude around 5.3 GHz increased the most as the clock misalignment increased. This is due to the presence of FM-to-AM conversion component which occurred at bit transitions. Note that only a difference of 2.63 dB at 10.6 GHz is obtained between perfect alignment and total misalignment, and that is why the clock frequency is not a good choice to achieve a high dynamic range.

Fig. 3.8 shows the monitored power at 5.3 GHz as a function of timing misalignment, while the CW laser frequency is aligned to the -3 dB point of the optical filter at its positive slope. The detection bandwidth is the resolution bandwidth of the spectrum analyzer, 300 kHz. Furthermore, the detected RF power should be averaged over time to prevent the pattern dependent effect induced by consecutive data transitions. A dynamic range of ~17.5 dB was achieved within a range of ±40 ps. This is a much higher monitoring sensitivity when compared with the results given in [21], [22]. The corresponding 10.61 Gb/s RZ-DPSK system power penalty induced by the timing misalignment is also shown in Fig. 3.8. Note that the power penalty increases rapidly when the timing misalignment exceeds ±15 ps. The degraded eye diagrams for various timing misalignment are shown in Fig. 3.9, respectively.

Fig. 3.10 shows the optical thin-film filter frequency response obtained from an optical amplifier-based white noise source. The corresponding monitoring power dynamic range as a function of frequency detuning between the CW laser frequency and optical filter center frequency is also shown. A dynamic range of more than 15 dB can be achieved at either slopes of the optical filter within a wide detuning range of >0.3 nm. Note that when the laser frequency was aligned to the center of the optical filter, the dynamic range was severely degraded. This is because the flat top response cannot provide enough FM-to-AM conversion. In addition, the dynamic range was also severely reduced when the laser frequency is tuned to the edge of the optical filter, because in this case, the measured dynamic range was limited by the high optical filter insertion loss (> 30 dB).

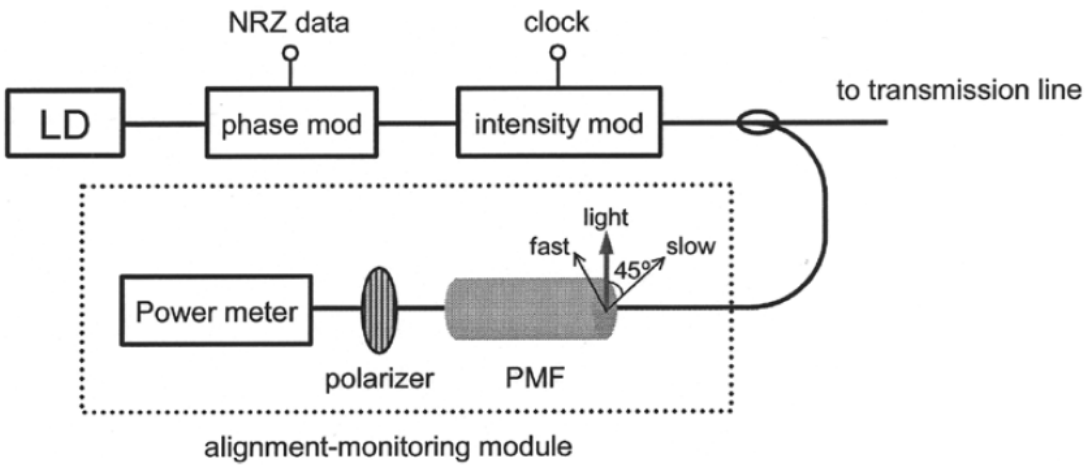

Fig. 3.1 Schematic diagram of alignment-monitoring module using DOP method [21].

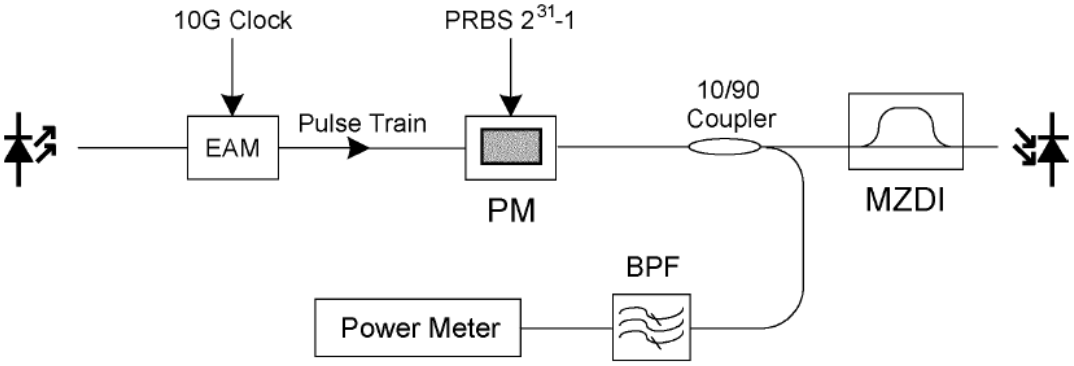

Fig. 3.2 Schematic diagram of alignment-monitoring module using off-center filtering method [22].

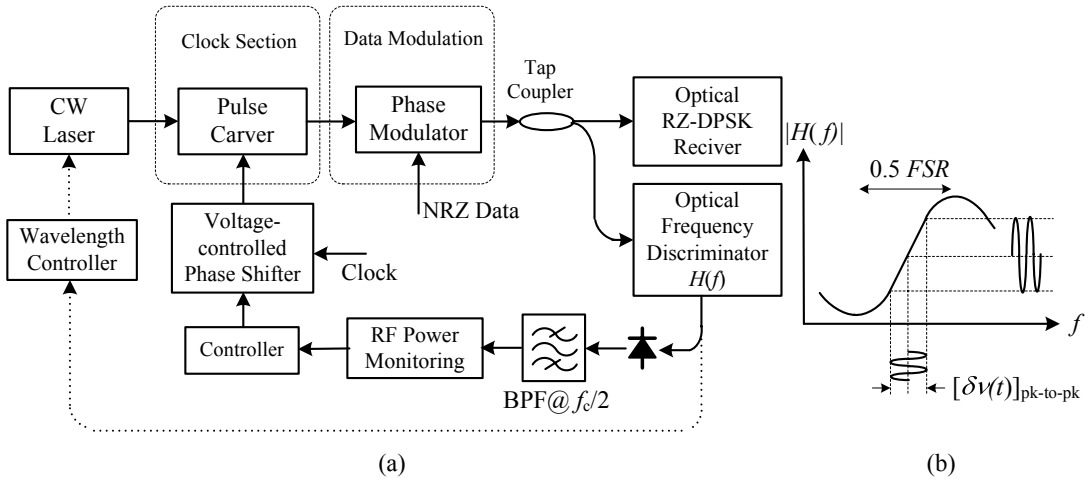

Fig. 3.3 (a) Proposed setup for monitoring clock misalignment. (b) Frequency-to-intensity conversion characteristic of a delay-and-add discriminator.

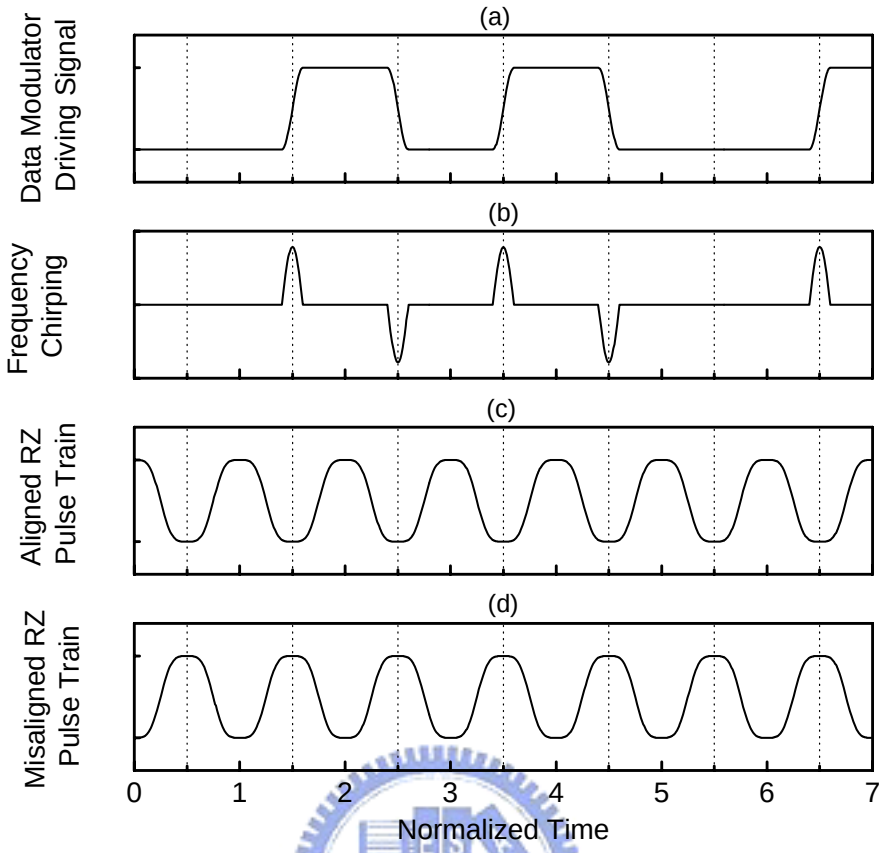

Fig. 3.4 Illustration of the timing alignment between a pulse carver and a data modulator. (a) Data modulator driving signal. (b) Frequency chirp duo to data transitions. (c) RZ pulse train with perfect timing alignment. (d) RZ pulse train with misaligned timing.

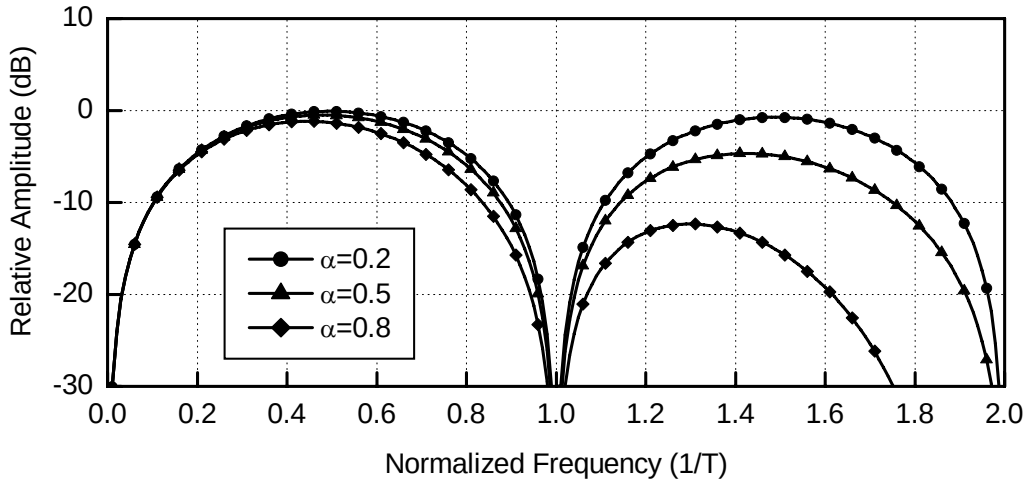

Fig. 3.5 RF spectra of (3–4) for various roll-off factors α of the phase modulator driving pulse *m(t)*.

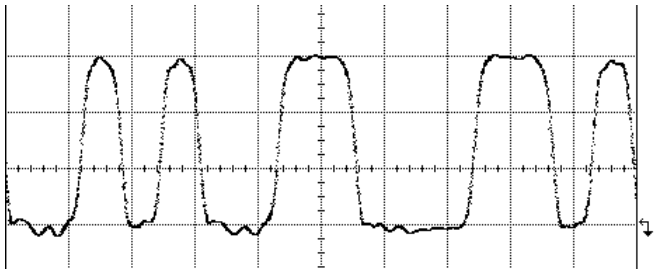

(a)

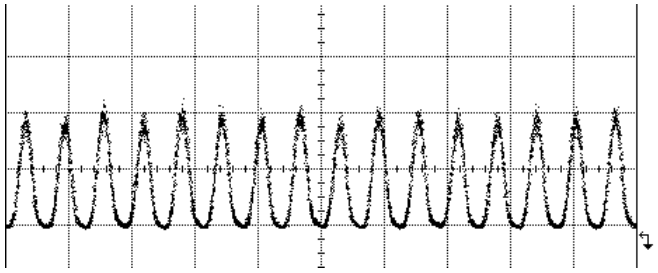

(b)

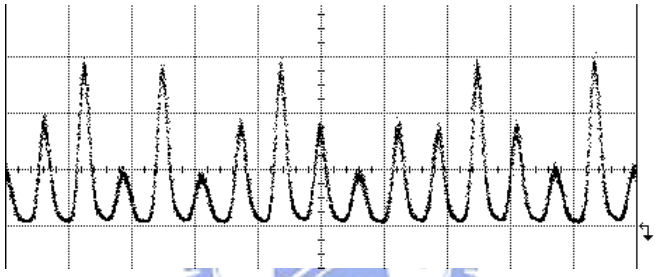

(c)

Fig. 3.6 Measured driving signal of the phase modulator (a), detected RZ pulses using the proposed method with a clock misalignment of 0 ps (b), and 47 ps (c), respectively.

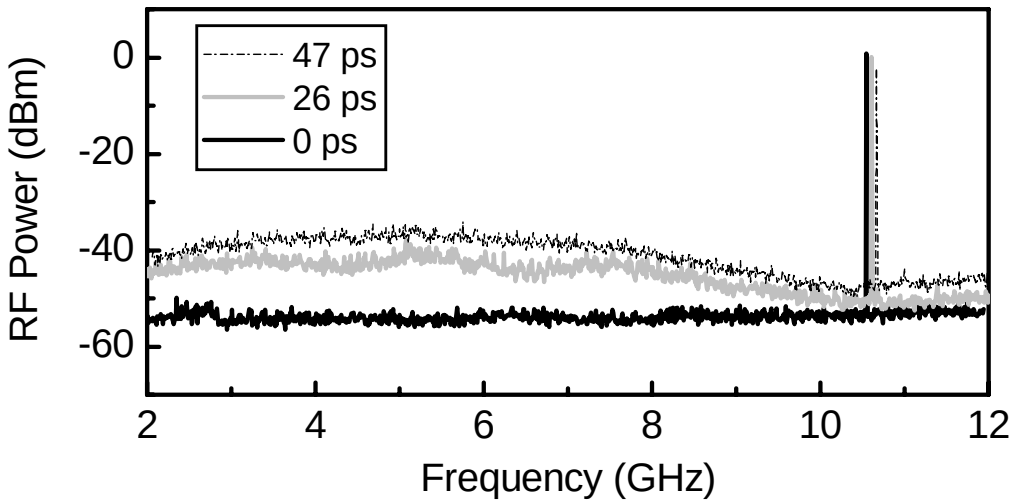

Fig. 3.7 The measured RF spectrum of a 10.61 Gb/s RZ-DPSK signal through an optical frequency discriminator with a clock misalignment of 0, 26 and 47 ps. The optical carrier frequency is aligned to the -3 dB point of an optical thin-film filter at its positive slope. The RF spectrum analyzer resolution and video bandwidths were both 300 kHz.

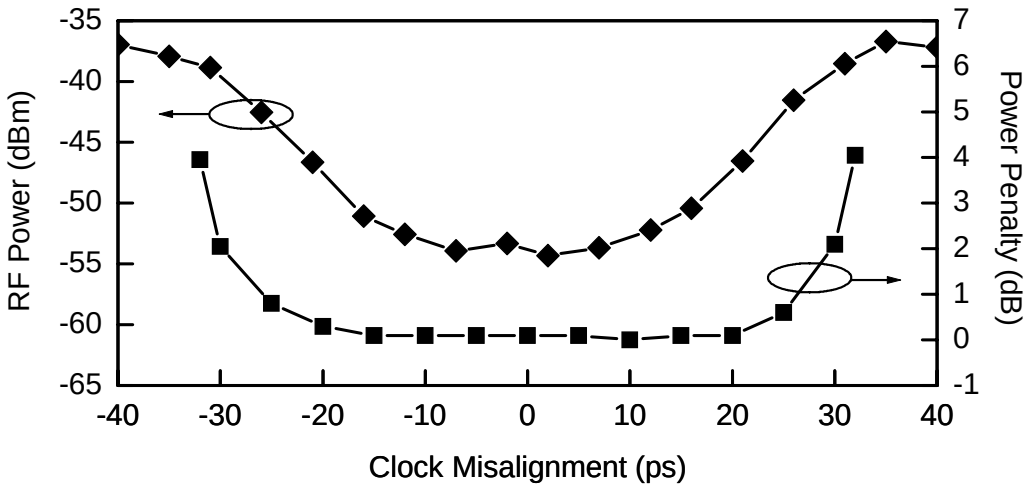

Fig. 3.8 The monitored power at 5.3 GHz as a function of timing misalignment and the corresponding power penalty of the 10.61 Gb/s RZ-DPSK signal.

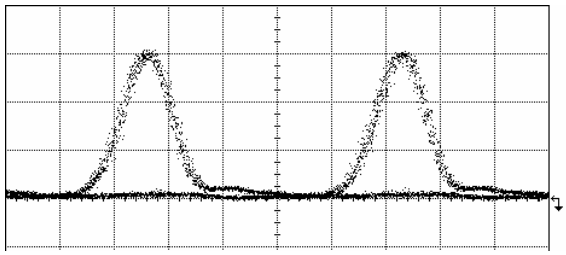

(a)

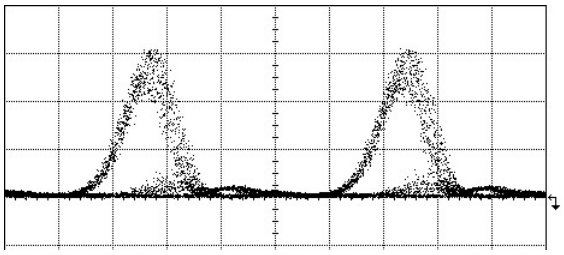

(b)

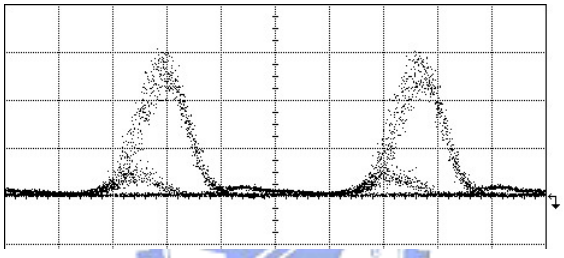

(c)

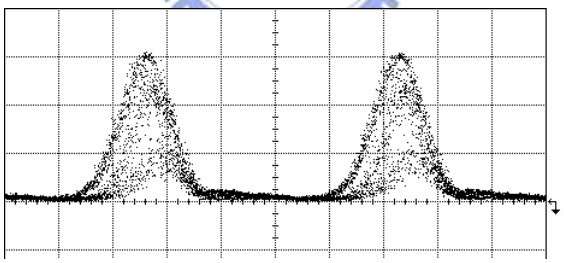

(d)

Fig. 3.9 Degraded eye diagrams due to misalignment with (a) 0 ps, (b) 32 ps, (c) -32 ps, and (d) 47 ps. (Units in X axis: 20 ps/div)

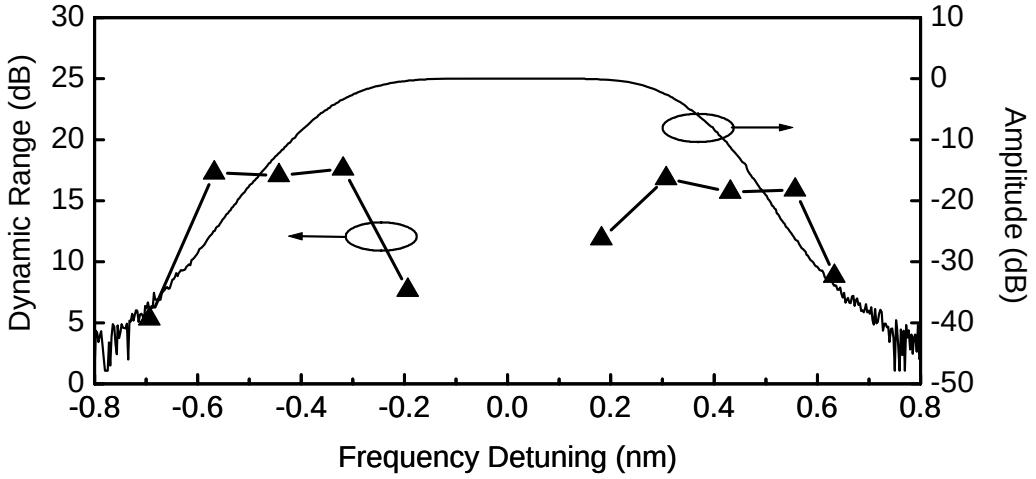

Fig. 3.10 The monitored power dynamic range as a function of the frequency detuning between the CW laser and the center frequency of the optical filter (left-hand side Y-axis), and the corresponding frequency response of the optical thin-film filter (right-hand side Y-axis).

Chapter 4 Electro-Optical Pre-distortion Technique

4.1 Introduction

The sinusoidal light versus bias voltage (L-V) transfer curve of a $LiNbO_3$-based external modulator prevents a multi-channel CATV system from obtaining a highly linear performance. Presently, however, external modulator-based transmitters are linear enough to transport > 80 channels of AM video signals, because an electrical pre-distortion technique with two arrangements has been successfully used. The first arrangement is that the bias point of the external modulator is fixed at the inflection point of the sinusoidal L-V curve [24] so that second-order nonlinear distortions (NLDs) can be completely suppressed. The second arrangement is that a third- and/or fifth-order pre-distortion circuit is inserted between the modulating signal source and the external modulator, so that the major odd-order NLDs can be suppressed significantly. However, even when this highly linear optical transmitter is used in an optical fiber CATV system, the performance of the entire system can still exhibit high composite second order (CSO) because many other NLD-generation mechanisms may exist. For examples, CSOs can be generated from optical receivers, semiconductor optical amplifiers (SOAs), linear optical fiber dispersions [25],[26], self-phase modulations [25–27], interferometric multiple reflections [28],[29], etc. Therefore, it may be preferred to design an optical transmitter that can provide a highly linear performance for the end-to-end system. In other words, the optical transmitter can itself generate certain levels of NLDs, in order to compensate the NLDs generated from the transmission system.

In this letter, we propose a novel pre-distortion technique in an external modulation system. This technique is used to compensate the frequency-independent CSO products generated from the transmission link. The basic idea of this technique is to shift the bias point of an external modulator from its inflection point so that transmitter-generated CSO products can be used to cancel those from the system. We experimentally demonstrate the feasibility of this technique by using a 1.3 μm-external modulator-based transmitter whose bias voltage is offset from the inflection point. The transmitter-generated CSOs can be used to compensate those generated from a 1.3 μm semiconductor optical amplifier.

4.2 Operation Principle

The operation principle of the proposed technique is explained in this Section. We start with the static transfer characteristic of an MZI modulator given by

$$P_{out}(t)=\frac{P_{in}L_a}{2}\left[1+\sin\left(\frac{\pi}{V_\pi}V(t)+\phi\right)\right] \tag{4-1}$$

where P_{out} is the output power of the MZI modulator, P_{in} is the input power of the MZI modulator, L_a is the insertion loss due to the MZI modulator, $V(t)$ is the modulating voltage, V_π is the half wave voltage of the MZI modulator (the voltage required to achieve 180^o optical phase shift), and ϕ is static bias phase shift. Assume that the modulating voltage $V(t)$ is composed of multiple channels of CATV signals and a DC bias voltage V_b:

$$V(t)=\sum_{i=1}^{N}A\sin(\omega_i t+\theta_i)+V_b \tag{4–2}$$

where A is the amplitude and ω_i is the angular frequency of the i-th channel. By substituting Eq.(4–2) into Eq.(4–1), the AC output of the MZI modulator can be expanded as

$$\begin{aligned}&\frac{P_{in}L_a}{2}\sin\left(\frac{\pi}{V_\pi}V(t)+\phi\right)\\&=\frac{P_{in}L_a}{2}\left\{\sin\left(\frac{\pi}{V_\pi}V_b+\phi\right)\cos\left(\frac{\pi}{V_\pi}\sum_{i=1}^{N}A\sin(\omega_i t+\theta_i)\right)+\cos\left(\frac{\pi}{V_\pi}V_b+\phi\right)\sin\left(\frac{\pi}{V_\pi}\sum_{i=1}^{N}A\sin(\omega_i t+\theta_i)\right)\right\}\end{aligned} \tag{4–3}$$

Let $\chi=\frac{\pi}{V_\pi}A$, we can use Bessel function expansions to obtain

$$\begin{aligned}&\sin\left(\frac{\pi}{V_\pi}\sum_{i=1}^{N}A\sin(\omega_i t+\theta_i)\right)\\&=\left\{\sum_{n_1=-\infty}^{\infty}\sum_{n_2=-\infty}^{\infty}\cdots\sum_{n_N=-\infty}^{\infty}J_{n_1}(\chi)J_{n_2}(\chi)\cdots J_{n_N}(\chi)\sin[n_1(\omega_1 t+\theta_1)+n_2(\omega_2 t+\theta_2)\cdots+n_N(\omega_N t+\theta_N)]\right\}\end{aligned} \tag{4–4}$$

$$\cos\left(\frac{\pi}{V_\pi}\sum_{i=1}^{N} A\sin(\omega_i t+\theta_i)\right)$$
$$=\left\{\sum_{n_1=-\infty}^{\infty}\sum_{n_2=-\infty}^{\infty}\cdots\sum_{n_N=-\infty}^{\infty}J_{n_1}(\chi)J_{n_2}(\chi)\cdots J_{n_N}(\chi)\cos[n_1(\omega_1 t+\theta_1)+n_2(\omega_2 t+\theta_2)\cdots+n_N(\omega_N t+\theta_N)]\right\} \quad (4\text{–}5)$$

where J_n is the n-th order Bessel function of the first kind. From Eqs. (4–3)–(4–5), we can obtain the fundamental carrier amplitude by letting $n_i=1$, $n_{j,j\neq i}=0$ to be

$$\frac{P_{in}L_a}{2}\left\{2J_1(\chi)[J_0(\chi)]^{N-1}\cos\left(\frac{\pi}{V_\pi}V_b+\phi\right)\right\} \quad (4\text{–}6)$$

The amplitude of the second-order intermodulation of the type $\omega_i+\omega_j$ is given by

$$\frac{P_{in}L_a}{2}\left\{2[J_1(\chi)]^2[J_0(\chi)]^{N-2}\sin\left(\frac{\pi}{V_\pi}V_b+\phi\right)\right\} \quad (4\text{–}7)$$

and the amplitude of the third-order intermodulation of the type $\omega_i+\omega_j-\omega_k$ is given by

$$\frac{P_{in}L_a}{2}\left\{2[J_1(\chi)]^2 J_{-1}(\chi)[J_0(\chi)]^{N-3}\cos\left(\frac{\pi}{V_\pi}V_b+\phi\right)\right\} \quad (4\text{–}8)$$

Therefore, the power ratio of carrier to CSO is given by

$$\frac{C}{CSO}=\frac{\left\{2J_1(\chi)[J_0(\chi)]^{N-1}\right\}^2}{\left\{2[J_1(\chi)]^2[J_0(\chi)]^{N-2}\right\}^2 N_{CSO}}\cot^2\left(\frac{\pi}{V_\pi}V_b+\phi\right)$$
$$=\frac{1}{N_{CSO}}\left\{\frac{J_0(\chi)}{J_1(\chi)}\right\}^2\cot^2\left(\frac{\pi}{V_\pi}V_b+\phi\right) \quad (4\text{–}9)$$
$$\cong\frac{1}{N_{CSO}}\left(\frac{2}{\chi}\right)^2\cot^2\left(\frac{\pi}{V_\pi}V_b+\phi\right)$$

where *Ncso* is the product-count of CSO. The power ratio of carrier to composite triple beat (CTB) is given by

$$\frac{C}{CTB} = \frac{\left\{2J_1(\chi)[J_0(\chi)]^{N-1}\right\}^2}{\left\{-2[J_1(\chi)]^3[J_0(\chi)]^{N-3}\right\}^2 N_{CTB}}$$
$$= \frac{1}{N_{CTB}}\left\{\frac{J_0(\chi)}{J_1(\chi)}\right\}^4 \qquad (4\text{–}10)$$
$$\cong \frac{1}{N_{CTB}}\left(\frac{2}{\chi}\right)^4$$

where N_{CTB} is the product-count of CTB. From Eqs.(4–9) and (4–10), we can calculate the *C/CSO* and *C/CTB* as a function of bias voltage offset (from inflection point) for any number of input carriers. Fig. 4.1 is the result for single-tone input (with an optical modulation index or OMI equals to 0.6), and Fig. 4.2 is the result for two-tone input (each with an OMI equals to 0.2). It is clear from Fig. 4.1 that when the bias point is at mV_π (m=0, ±1, ±2, ...), we can obtain the best carrier to second-order harmonic distortion ratio, as expected. From Fig. 4.2, we can see that when the bias voltage is offset slightly from the inflection point, the second-order NLDs increase sharply, while the third-order NLDs decrease slowly. For example, for a bias offset of $0.1V_\pi$, the $\omega_1+\omega_2$ components increase from non-existent to about –30 dBc, and both the fundamental carrier and the $\omega_1+2\omega_2$ component decrease by 0.44 dB (i.e., *C/CTB* remains constant). The small change of fundamental carrier power indicates that the change of OMI depends critically on the final bias point, i.e., OMI can be increased or decreased, depending on if the DC offset gives lower or higher optical power. On the right axis of Fig. 4.2, we also see that when the offset is positive, the DC power can be increased (up to 3 dB). For example, for a $0.1V_\pi$ offset, the DC power increases by about 1.15 dB.

To summarize our analysis so far: when the bias voltage is offset from the inflection point, the resultant CSOs can be increased significantly, and they can be used to compensate the CSOs generated from the transmission system. In the mean time, the changes of the resultant CTB is small, while CNR and DC power can vary depending on the offset direction.

Although we have proved that significant CSOs can be generated from the optical transmitter by offsetting the bias from inflection point, we cannot be sure about whether the phase of these CSOs are in or out of phase with respect to the transmission system-generated CSOs. Fortunately, we note that we can change the sign of the CSOs by changing the direction of bias offset. For instance, the CSOs due to +0.1 and $-0.1V_\pi$ offsets are 180° out of phase with respect to each other.

4.3 Experimental Results

The Experimental setup is shown in Fig. 4.3. Seventy-seven random-phased continuous-wave (CW) carriers with 6 MHz spacing (starting from 55.25 MHz), from a matrix generator were used to modulate a 1.3 μm $LiNbO_3$ balanced bridge interferometer (BBI) CATV modulator, which has dual outputs. By using a 1.3 μm distributed-feedback (DFB) laser, both optical outputs of the modulator reached 3.5 dBm. The optical modulation index per channel (OMI/ch) is about 3%. The BBI modulator had a bias control circuit to control and to stabilize the modulator's bias point. It should be noted that the conventional Schottky diode-based pre-distortion circuit [24] was not used. Between the external modulator and the optical receiver are two adjustable optical attenuators, a commercial available multiple-quantum-well (MQW) SOA, and two optical isolators before and after the MQW-SOA to minimize the multiple reflection effect. The MQW-SOA had a low polarization sensitivity (~0.5 dB) and a low gain ripple performance (< 0.3 dB). At a bias current of 300 mA, the MQW-SOA had a fiber-to-fiber gain of 28.9 dB with a gain peak at 1310 nm. When the SOA input power level was at –14.3 dBm and the modulator was bias at the inflection point, the received RF spectra at three different frequency bands are shown in Fig. 4.4(a). The three frequency bands include those channels at low-frequency range (50-100 MHz), middle-frequency range (290-330 MHz), and high-frequency range (520-560 MHz). We can see that the worst case *C/CSO* in the three frequency bands were 18, 24, and 23 dB, respectively. After the modulator bias point was offset by 0.24 V_π, the worst case *C/CSO* in all three frequency bands were significantly improved to 34, 40, and 32 dB, respectively, as can be observed in Fig. 4.4(b). These results can indeed demonstrate the feasibility of our proposed linearization technique.

4.4 Discussions

Comparing the CNR before and after the bias offset of 0.24 V_{π}, we can see in Figs. 4.4(a) and 4.4(b) that the CNR was improved by about 4 dB in the latter case. This is because when the optical power was lowered, the OMI/ch was increased and the shot noise level was decreased, and both contribute to increase the resultant CNR.

Another point worth emphasizing is that, for a BBI modulator with dual outputs, when we change the bias point to cancel the CSOs generated in the transmission system, only one of the dual outputs can work effectively. This is because the CSOs generated from the two BBI outputs are 180^{o} out of phase. This phenomenon implies that this technique is best applied to an MZI with a single output.

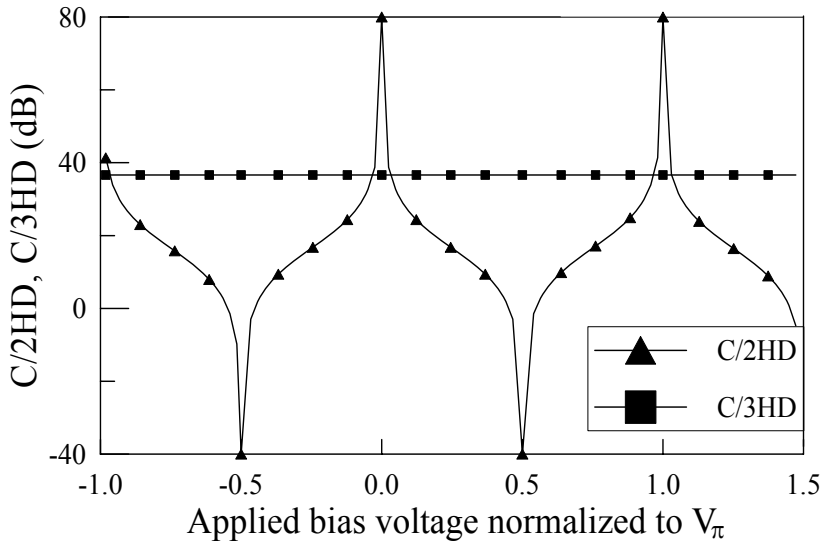

Fig. 4.1 C/2HD, C/3HD versus applied bias voltage when the MZI modulator is modulated by a single tone with an OMI = 0.6.

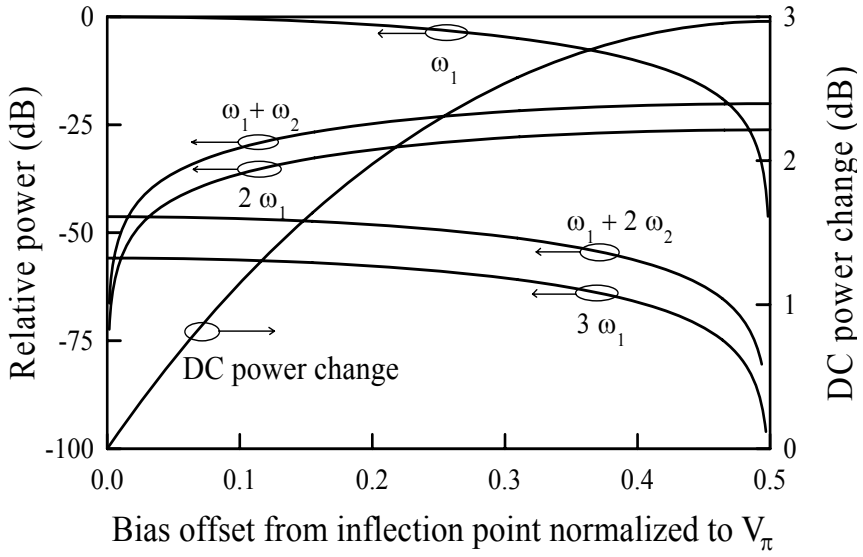

Fig. 4.2 Relative power and DC power change versus the bias offset from inflection point. The MZI modulator is modulated by two tones (OMI/tone = 0.2).

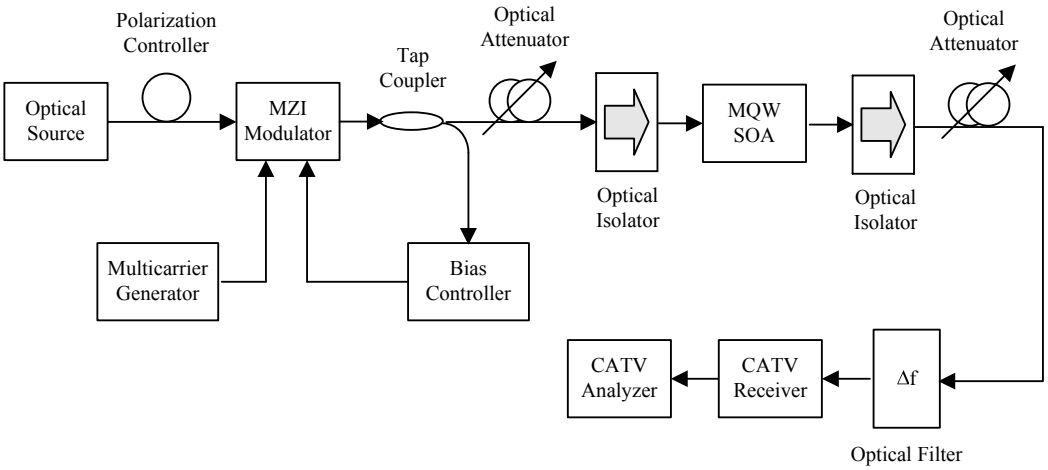

Fig. 4.3 The experimental setup to demonstrate the SOA carrier-modulation- induced CSOs were suppressed over the entire CATV band by offsetting the bias point of a MZI modulator from its inflection point.

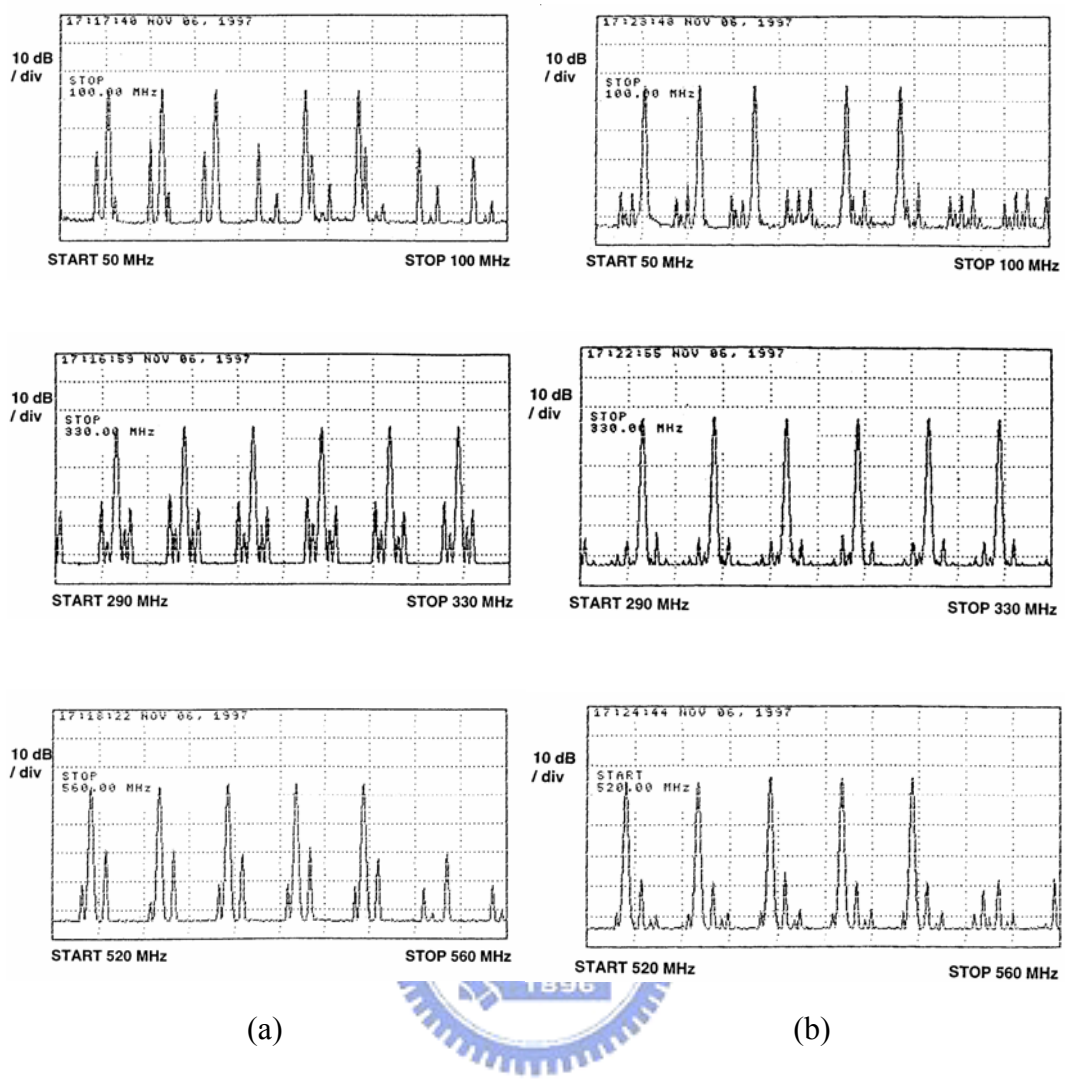

Fig. 4.4 The received RF spectra of an externally-modulated system with an in-line MQW-SOA when the MZI modulator is biased at (a) inflection point and (b) 0.24 V_π offset from the inflection point, respectively. (Top: 50~100 MHz, Middle: 290~ 330 MHz, Bottom: 520~560 MHz) (Resolution bandwidth = 100 kHz)

Chapter 5 Conclusions

In order to increase network capacity and achieve longer transmission distance, advanced optical performance monitoring and mitigation techniques provide promising solutions. These techniques can improve the control of transmission and physical layer fault management, and they are essential in building a high capacity and reliable all-optical network, which are expected to be transparent and dynamic reconfigurable. However, technology challenges exist to achieve these goals. In this dissertation, we propose and demonstrate three novel techniques for optical performance monitoring and impairment mitigation. The major contribution of this dissertation are summarized as follows.

In Chapter 2, an adaptive post-detection method is proposed for chromatic dispersion monitoring. The method uses an optical delay-and-add filter, whose two arms have a differential optical delay equal to a half period of a pilot tone or a half-data-bit/one-data-bit period. This method does not require a pilot tone if the transmitted data has a symmetrical spectrum with respect to its optical carrier. Adaptive feedback schemes, such as a scheme to accurately align the DAF quadrature point with the optical carrier of a monitored wavelength and a scheme to automatically adjust a VDC based on the monitored clock or pilot-tone power, are proposed to form a complete dispersion equalization apparatus. We have shown that the post-detection scheme works well even when a residual chirp exists due to a finite MZ modulator DC extinction ratio or SPM. The proposed scheme was also verified by VPI simulation to work well for various modulation formats such as NRZ, RZ50, CS-RZ, RZ-DPSK and CSRZ-DPSK. The dependence of the dispersion monitoring window and dispersion resolution on data formats has also been thoroughly studied.

In Chapter 3, we have experimentally demonstrated an automatic timing alignment method for an RZ-DPSK transmitter using an optical frequency discriminator. Compared with previously published monitoring schemes, our proposed method achieved a significantly improved monitoring power dynamic range of ~17.5 dB within a timing alignment range of a half-bit period. An additional advantage of this method is that the optical frequency discriminator can also serve as a wavelength locker if the discriminator is temperature stabilized.

In Chapter 4, we have also demonstrated, both analytically and experimentally, that by offsetting the bias point of a MZI modulator from its inflection point, one can

obtain sufficient CSOs from the MZI-based transmitter to compensate those CSOs generated from an in-line SOA. The SOA carrier-modulation-induced CSOs were suppressed by as much as 9 to 16 dB over the entire CATV band (from 50 to 550 MHz). We believe that the same technique can also be applied to electro-absorption modulators.

The research can be studied consequently in following aspects.

(a) We have demonstrated our proposed chromatic dispersion monitoring technique by 10.61 Gb/s RZ signal and a half-bit-delay DAF. In addition, one published result [20] shows its feasibility using 10 Gb/s NRZ signal and an one-bit delay DAF. It is worthy to carry out experiments for various DAF differential delay and modulation formats, which have attracted much attention recently.

(b) For our proposed alignment monitoring technique for pulse carver and data modulator by using an optical frequency discriminator, the demonstrated experiment shows flat-top response of an optical filter will degrade the monitored power dynamic range, and therefore make the monitoring results more sensitivity to the filter center frequency stability. In order to increase the detuning range between the optical carrier frequency and center wavelength of the optical frequency discriminator, other optical filters can be used to replace the thin-film filter in our previous experiment. In our simulation, both Fabry Perot and Gaussian filters are good candidates for achieving this goal, as shown in Fig. 5.1. An experiment can be performed to verify its feasibility.

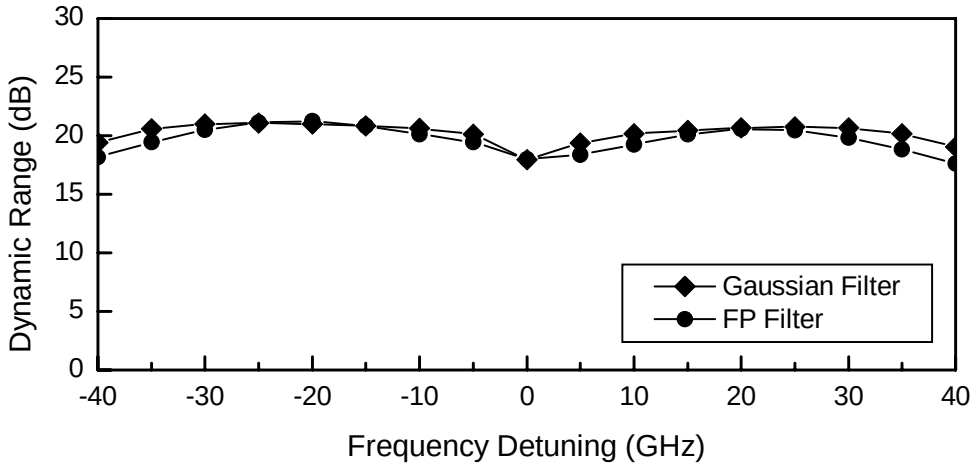

Fig. 5.1 Simulated Monitored power dynamic range (MPDR) as a function of the frequency detuning between the CW laser and the center frequency of the optical filter using Gaussian filter and Fabry Perot filter, respectively.

References

[1] D. C. Kilper, R. Bach, D. J. Blumenthal, D. Einstein, T. Landolsi, L. Ostar, M. Preiss, and A. E. Willner, "Optical performance monitoring," *J. Lightwave Technol.*, vol. 22, pp. 294-304, Jan. 2004.

[2] L. K. Chen, M. H. Cheung, and C. K. Chan, "From Optical Performance Monitoring to Optical Network Management: Research Progress and Challenges," *International Conference on Optical Communications and Networks, ICOCN 2004, (Invited Paper), Hong Kong,* Nov. 2004.

[3] Z. Pan, Y. Wang, Y. Song, R. Motaghian, S. Havstad, A. Willner, " Monitoring chromatic dispersion and PMD impairments in optical differential phase-shift-keyed (DPSK) systems," in *Proc. OFC'2003*, Paper. WP1, Mar 2003.

[4] S. M. Reza Motaghian, T. Luo, J. E. McGeehan, and A. E. Willner, "Enhancing the monitoring range and sensitivity in CSRZ chromatic dispersion monitors using a dispersion-biased RF clock tone," *IEEE Photon. Technol. Lett.*, vol. 16, pp. 1391-1393, May 2004.

[5] M. N. Petersen, Z. Pan, S. Lee, S. A. Havstad, and A. E. Willner, "Dispersion monitoring and compensation using a single inband subcarrier tone," in *Proc. OFC'2001*, pp. WH4-1 -WH4-3, Mar 2001.

[6] C. Youn, "Effects of SPM and PMD on chromatic dispersion monitoring techniques using pilot tones," in *Proc. OFC'2003*, Paper. WP2, Mar 2003.

[7] G. Ishikawa and H. Ooi, "Demonstration of automatic dispersion equalization in 40-Gbit/s OTDM transmission," *Proc. ECOC'98*, pp. 519-520, Sep. 1998.

[8] A. Sano, T. Kataoka, M. Tomizawa, K. Hagimoto, K. Sato, K. Wakita, and K. Kato, "Automatic dispersion equalization by monitoring extracted-clock power level in a 40-Gbit/s, 200-km transmission line," *Proc. ECOC'96*, vol. 2, pp. 207-210, 1996.

[9] Z. Pan, Q. Yu, Y. Xie, S. A. Havstad, A. E.Willner, D. S. Starodubov, and J. Feinberg, "Chromatic dispersion monitoring and automated compensation for NRZ and RZ data using clock regeneration and fading without adding signaling," *Tech. Dig. OFC'2001*, Mar. 2001.

[10] Z. Pan, Y. Wang, Y. Song, R. Motaghian, S. Havstad, A. Willner, " Monitoring chromatic dispersion and PMD impairments in optical differential phase-shift-keyed (DPSK) systems," in *Proc. OFC'2003*, Paper. WP1, Mar 2003.

[11] Y. Wang, Z. Pan, A. Sahin, L. Yan, C. Yu, A. Willner, "In-line chromatic dispersion monitoring using optically-added phase-modulated in-band tones for 10 Gb/s system," in *Proc. OFC'2003*, Paper. WP3, Mar 2003.

[12] S. Kuwahara, A. Sano, K. Yonenaga, Y. Miyamoto, and H. Toba, "Automatic dispersion equalization with simple zero dispersion detection using alternating chirp signal in 20-Gbit/s, 400-km transmission experiment," *Proc. OECC '99*, pp. 383-386, Oct. 1999.

[13] G. Rossi, T. E. Dimmick, and D. J. Blumenthal, "Optical performance monitoring in reconfigurable WDM optical networks using subcarrier multiplexing," *J. Lightwave Technol.*, vol. 18, pp. 1639-1648, Dec. 2000.

[14] K. Tatsuno, M. Shirai, H. Furuichi, K. Kuroguchi, N. Baba, H. Kuwano, Y. Iwafuji, and A. Murata, "50 GHz spacing, multi-wavelength tunable locker integrated in a transmitter module with monolithic-modulator and a DFB-laser," *Optical Fiber Communications Conf. Proc.*, Mar. 2001, pp. TuB5-1 - TuB5-4.

[15] A. Hodzic, B. Konrad, and K. Petermann, "Alternative modulation formats in Nx40 Gb/s WDM standard fiber RZ-transmission systems," *J. Lightwave Technol.*, vol. 20, pp. 598-607, Apr. 2002.

[16] S. Walklin and J. Conradi, "Effect of Mach–Zehnder modulator DC extinction ratio on residual chirp-induced dispersion in 10-Gb/s binary and AM-PSK duobinary lightwave systems," *IEEE Photon. Technol. Lett.*, vol. 9, pp. 1400-1402, Oct. 1997.

[17] H. Kim and A. H. Gnauck, "Chirp characteristics of dual-drive Mach–Zehnder modulator with a finite dc extinction ratio," *IEEE Photon. Technol. Lett.*, vol. 14, pp. 298-300, Mar. 2002.

[18] G. P. Agrawal, *Nonlinear Fiber Optics*. San Diego: Academic, 1989.

[19] K. J. Park, C. J. Youn, J. H. Lee, and Y. C. Chung, "Chromatic dispersion monitoring technique in WDM network," in *Tech. Dig. OFC 2002*, Anaheim, CA, Mar. 2002, Paper ThGG88.

[20] A. Campillo, "Chromatic dispersion-monitoring technique based on phase-sensitive detection," *IEEE Photon. Technol. Lett.*, vol. 17, pp. 1241-1243, June 2005.

[21] Hoon Kim, C. R. Doerr, R. Pafchek, L. W. Stulz, and P. Bernasconi, "Alignment monitoring of the pulse carver and data modulator for RZ-DPSK systems," *IEEE Photon. Technol. Lett.*, vol. 15, no. 11, pp. 1594-1596, Nov. 2003.

[22] Guo-Wei Lu, Yuen-Ching Ku, Lian-Kuan Chen, and Chun-Kit Chan, "A novel technique for pulse-carver and data alignment monitoring in RZ-DPSK systems using off-center optical filtering," *IEEE Photon. Technol. Lett.*, vol. 17, no. 3, pp. 711-713, Mar. 2005.

[23] J. H. Sinsky, "High-speed data and pulse-carver alignment in dual Mach–Zehnder modulator optical transmitters using microwave signal processing," *J.*

Lightw. Technol., vol. 21, no. 2, pp. 412-423, Feb. 2003.

[24] M. Nazarathy, J. Berger, A. J. Ley, I. M. Levi, and Y. Kagan, "Progress in externally modulated AM CATV transmission systems," *J. Lightwave Technol.*, vol 11, pp. 82-105, Jan. 1993.

[25] M. R. Plillips, T. E. Darcie, D. Marcuse, G. E. Bodeep, and N. J. Frigo, "Nonlinear distortion generated by dispersive transmission of chirped intensity-modulated signals," *IEEE Photon. Technol. Lett.*, vol. 3, no. 5, pp. 481-483, May 1991.

[26] W. H. Chen, M. C. Wu, C. T. Chang and W. I. Way, "Self-phase-modulation-limited transmission distance of repeaterless 1.55 μm multi-channel AM-VSB external modulation systems," *Conf. Proc.*, paper 3420-21, Photonics Taiwan, July 1998.

[27] C. Desem, "Composite second order distortion due to self-phase modulation in externally modulated optical AM-SCM systems operating at 1550 nm," *Electron. Lett.,* vol. 30, no. 24, pp. 2055-2056, Nov. 1994.

[28] W. I. Way, *Broadband HFC Access System Technologies: Subcarrier Multiplexed Lightwave Systems, RF Modems, and MAC Protocols*, Academic Press Inc., 1998.

[29] J. H. Angenent, I. P. D. Ubbens, P. J. de Waard, "Distortion of a multicarrier signal due to optical reflections," *Technical Digest, ECOC'91*, paper WeC8-4, Paris, France, Sept. 1991.